Failure Analysis and Design of a Heavily Loaded Pin Joint

by

Nader Farzaneh

Submitted to the Department of Mechanical Engineering
in partial fulfillment of the requirements for the degree of

Master of Science in Mechanical Engineering

at the

MASSACHUSETTS INSTITUTE OF TECHNOLOGY

June 2002

Author ....
Department of Mechanical Engineering
March 27, 2002

Certified by.......................
Samir Nayfeh
Assistant Professor
Thesis Supervisor

Accepted by........................
Ain Sonin
Chairman, Department Committee on Graduate Students
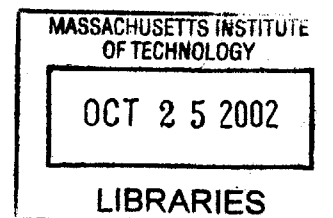
Failure Analysis and Design of a Heavily Loaded Pin Joint

by

Nader Farzaneh

Submitted to the Department of Mechanical Engineering
on March 27, 2002, in partial fulfillment of the
requirements for the degree of
Master of Science in Mechanical Engineering

Abstract

Plain sliding bushings and pins are often employed to create pin joints in heavy machinery. At high loads and low speeds, such bearings operate in the regime of boundary lubrication, and are prone to failure by galling, which involves a transfer of material between the pin and bushing. This thesis comprises a theoretical and experimental study of the stress and lubricant distribution plain pin and bushing pairs.

A finite-element study is conducted to determine the contact stress distribution at the interface of the pin and bushing, and comparisons are made to the Hertz contact theory. We compare the stresses computed for a straight pin and bushing to that computed for a bushing with lobes and a bushing with undercuts. The results suggest that an undercut bushing will have a significantly longer life than a straight or lobed bushing.

A test machine which exerts a radial force on a bushing and oscillates the joint through a fixed angle is developed. This machine is used to test steel pin-bushing pairs to failure and to conduct optical measurements of the oil film developed in acrylic pin-bushing pairs. Preliminary results of the tests are presented.

Thesis Supervisor: Samir Nayfeh
Title: Assistant Professor

Acknowledgments

First of all I would like to thank Professor Samir Nayfeh for giving me the opportunity to work with him and learn from his experience. He has introduced me to many different fields within machine design, which has given me a deep appreciation for the design process. His guidance and support has made my graduate experience enjoyable and productive.

I would like to acknowledge Greg Radighieri and Dhanush Mariappan for being such good 'teammates'. I learned much from Greg's knowledge in machine design, particularily through the stages of design on the pin joint test machine. I like to thank Carlos Hidrovo for teaching me the ERLIF process and also for training me on the laser and the optics that were used in the optical tests. Without Carlos, the optical testing on the pin joint would not be possible. I like to thank Dhanush for his help in conducting the experiments and in doing the image post-processing of the laser fluorescence.

I like to thank all the guys from the "MESOLAB", in particular Kripa Varanasi. Kripa would always take from his own time to answer my technical questions.

Most of all, I like to thank my parents for supporting me and encouraging me to be my best. Nothing that I can write here will show how much I appreciate them.

Contents

8

List of Figures

Chapter 1

Introduction

1.1 Background

One of the major components in heavy machinery is the pin joint. A pin joint connects two links by constraining the lateral movement while allowing rotation of the links. In heavy types of machinery, pin joints are often formed using a plain pin and bushing. Under heavy loads and slow rotational speeds, such a joint will operate in the boundary lubrication regime. Under such conditions, a steel-on-steel pin joint is prone to "galling" failure. Some of the possible reasons for galling include lack of lubrication, contact of similar metals, relative surface roughness of the mating parts, joint misalignment, and contamination. In this work we consider the feasibility of decreasing the contact stress in the pin-joint by modifying its design. By producing an undercut in the bushing, the contact stress between the pin and the bushing can be decreased. In order to test whether this decrease in stress actually results in a longer work life for the pin-joint, we conduct experiments under normal conditions. For the testing purposes, a machine is designed to load a pin joint and rotate it at the same time, which would test the pin joint close to its normal operating conditions.

11

1.2 Pin and Bushing Characteristics

The pin under study has a diameter of 66.7 mm, and a length of 350.8 mm (Figure 1-1). The bushing has a inside diameter of 67.88 mm and outside diameter of 106.6 mm, and is 237.3 mm long. The minimum clearance between the pin and the bushing at the center of the pin is 0.88 mm. The bushing also has two lobes on the inside diameter, which decreases the clearance between the pin and the bushing to 0.405 mm.

c
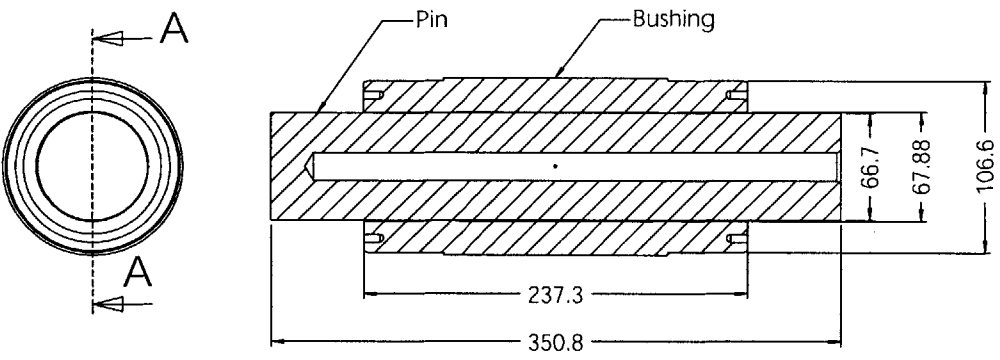
Figure 1-1: Pin Joint

Chapter 2

Failure Analysis of the Pin Joints

2.1 Failure Modes

The failure of pin joints has been studied closely and some of the failure modes analyzed include: loss of the lubricant, seizure of the pin, noise and vibration in the pin joint, loosening of the joint, yielding of the pin, and development of grooves in the bushing end surfaces.

The major reason for the loss of oil in the pin joint is the wear of the seal. The surface of the seal may also be damaged by abrasives. The seizure of the pin against the bushing may be caused by excessive loading, internal wear debris, and metal-to-metal contact. Wear debris decrease the clearance between the pin and the bushing and eventually cause a press-fit condition [17]. Noise and vibration in the pin joint can be caused by poor surface finish, excessive local contact pressure, and particle debris. The loose joint failure mode can be caused by excessive bore contact pressure, insufficient press fit, low material strength, and wear of the pin and the bushing. The yielding of the pin can be caused by the use of an undersized pin, incorrect design loads, and the center hole being oversized. The grooves may be caused by incorrect bushing end surface, hardness, and heat due to high seal velocity.

2.2 Tribology of the Pin and the Bushing

Tribology is defined as the science of interacting surfaces in relative motion [21].It encompasses the fields of friction, lubrication, and wear. Tribology is the fundamental science behind the wear mechanism of the pin joint, and thus the concepts associated with tribology are introduced in the following paragraphs.

2.2.1 Types of Wear

Wear is the loss of material from contacting bodies in relative motion. The are several factors influencing wear, including material properties, environmental conditions, and the geometry of the contacting bodies.

The first type of wear is adhesive wear, which arises from the formation of adhesive junctions at the contact region. Adhesive wear particles are formed through several stages [21]:

1. deformation of contacting asperities

2. removal of surface films

3. formation of adhesive junctions

4. failure of junctions and transfer of the material

5. modifications of transferred fragments

6. removal of fragments and formation of loose wear particles

The amount of the material removed due to adhesive wear can be estimated from

$$V_{adh} = k\frac{P}{H}L \tag{2.1}$$

where k is the wear coefficient, P is the load, H is the hardness of the softer material in contact, and L is the sliding distance.

Abrasive wear is another common type of wear which results from the penetration of the harder surface of the contacting materials into the softer surface. The result is

plastic deformation of the softer surface. Tangential motion results in micro-ploughing and micro-cutting, which removes material from the soft surface. An estimate of volume removed during abrasive wear is

$$V_{abr} = \frac{2}{\pi} \frac{\tan \Theta}{H} PL \tag{2.2}$$

where Θ is the slope of the asperity with respect to the surface.

Wear can also be caused by surface fatigue, which results from cyclic loading at the surface. Load cycling is especially common in rolling contact surfaces. The materials form cracks under their surfaces and, as the load cycle continues, the crack propagates and eventually creates wear particles. The amount of material removed due to fatigue can be expressed as

$$V_f = C \frac{\eta \gamma}{\epsilon^2 H} PL \tag{2.3}$$

where C is a constant, η is the distribution of asperity heights, γ is the particle size constant, and ϵ is the strain to failure in one load cycle. One type of contact fatigue is spalling fatigue, which results in a crater-like depression in the rolling surface [22]. Surface distress is another type of fatigue failure, which results in burnishing of the surface. The burnish is characterized by glossiness of the metal surface, which is believed to arise from plastic deformation of the asperities. As the failure advances, small pits form on the burnished surface.

The three types of wear mentioned in the foregoing are mechanical in nature, but wear can also be caused by chemical reactions. The chemical reaction can be initiated by friction between the two bodies, which increases the reactivity of the material due to an increase in temperature. The surface then reacts with the environment and reaction products are formed on the surface. Crack formation and abrasion removes these products from the surface and results in wear of the material.

For the wear mechanisms of adhesion, abrasion, and fatigue, the amount of material removed is directly proportional to the amount of load. The load on the asperities is a function of the contact stress between the two surfaces. Thus the rate of wear

15

associated with the mechanical processes can be decreased by reducing the contact stress between the surfaces.

2.2.2 Effects of Lubrication on Wear

The presence of lubricant between two surfaces can reduce the wear rate significantly. The lubricant separates the two surfaces so that there is no actual metal-to-metal contact, thus reducing the abrasive and adhesion wear in the pin joint. The lubricant also helps to remove wear particles between the surfaces and acts as a coolant for the contact surfaces. The effectiveness of lubricants can be reduced by heat and time, which cause the molecules of the lubricant to decompose. Thus the choice for a proper lubricant is critical in applications prone to surface failure.

Oil Viscosity

The most important parameter characterizing the lubricant is viscosity. Viscosity is defined as the ratio of the shear stress to the shear strain rate of the fluid, or

$$\eta = \frac{F/A}{v/h} \tag{2.4}$$

where F is the shear force, A is the area of the upper surface, v is the relative velocity of the surfaces, and h is the separation between the two surfaces [20]. The absolute viscosity ($\eta_k = \eta/\rho$) of 80W-90 oil, which is used in our study, is 1.4×10^{-4} m^2/s.

The viscosity of the oil is both pressure and temperature dependant. The viscosity-temperature relationship is most accurately modelled by the Vogel equation

$$\eta = ae^{b/(T-c)} \tag{2.5}$$

which illustrates that the viscosity decreases with increasing temperature. The value of the constants a, b, and c can be determined from experimental measurements.

The relationship between the viscosity and pressure is modelled as [20]

$$\eta_p = \eta_0 e^{\alpha p} \tag{2.6}$$

16

where α is the pressure-viscosity coefficient, and p is the pressure. Thus the viscosity of the lubricant increases with pressure. The viscosity of the oil should be high enough to support the load between the surfaces, but not so high that it results in excessive loss of power.

Lubrication Regimes

There are four regimes in which the lubricant operates. They include hydrodynamic, elastohydrodynamic, partial, and boundary lubrication.

In hydrodynamic lubrication, there is sufficient pressure in the oil film to support the load between the surfaces, and therefore there is no contact between the two solid surfaces. Hydrodynamic lubrication provides low friction and thus high resistance to wear.

Elastohydodynamic lubrication is a form of hydrodynamic lubrication, but the elastic deformation of the lubricated surfaces become significant. Elastohydrodynamic lubrication is normally associated with non-conformal surfaces, and thus is more applicable to rolling-element bearings. If there is sufficient rolling speed for the given load condition and lubricant, then the lubricant film is maintained between the two contacting surfaces. For high loads, the film is essentially of uniform thickness in the contact area.

In boundary lubrication, the surfaces are not separated by the lubricant, and thus there is asperity contact between the surfaces. The friction and wear is therefore dependent on the properties of the solid and the lubricant film. The wear rate and coefficient of friction of the boundary lubrication regime is much greater than that of hydrodynamic and elastohydrodynamic, but still significantly lower than the unlubricated case. The coefficient of friction can decrease by an order of magnitude in the transition from the unlubricated regime to the boundary lubrication regime [9]. This is because the lubricant film attaches to the surface by adsorption and supports the load by resistance to being squeezed from between the converging asperities [8]. At high temperatures, desorption of the oil film occurs, which results in metal-to-metal contact and a higher wear rate. The conditions under which boundary lubrication

exists include high loads, high temperatures, and low surface speeds [8].

The four lubrication regimes can be distinguished by using the film parameter Λ. The relationship between the film parameter and the minimum film thickness h_{min} separating the two bodies can be expressed as [9]

$$\Lambda = \frac{h_{min}}{(R_{qa}^2 + R_{qb}^2)^{\frac{1}{2}}} \tag{2.7}$$

where R_{qa}^2 is the rms surface roughness of surface a [1] a and R_{qb}^2 is the rms surface roughness of surface b.

The minimum film thickness formed in a line contact (cylinder on cylinder) can be expressed as [21]

$$h_{min} = 2.65 \frac{G^{0.54}V^{0.7}R}{W^{0.13}} \tag{2.8}$$

where

$G = \alpha E$: Dimensionless material parameter

$V = \frac{\eta v}{2ER}$: Dimensionless speed parameter

$W = \frac{w}{ERL}$: Dimensionless load parameter

$R = \frac{R_1 R_2}{R_1 - R_2}$

$E = (\frac{1-\nu_1^2}{E_1} + \frac{1-\nu_2^2}{E_2})^{-1}$

α : Pressure-viscosity coefficient of lubricant

v : Surface velocity

w : Contact load

η : Lubricant viscosity

L : Length of contact

---

[1] $R_a = (\frac{1}{N}\sum_{i=1}^{N} z_i^2)^{\frac{1}{2}}$

For the pin joint under study, the parameter values are:

$R_1 = 33.59$ mm (bushing radius)

$R_2 = 33.36$ mm (pin radius)

$w = 222.5$ kN

$E1 = E2 = 200$ GPa

$\nu_1 = \nu_2 = 0.3$

$v = 0.084$ m/s

$\eta = 0.12$ Pascal-seconds

$L = 237$ mm

Thus a pin joint loaded at 100,000 lbf and running at an angular speed of 2.5 radians/second, has a minimum film thickness (h_{min}) of 0.54 micrometers and a film parameter (Λ) value of 1.52×10^{-6}.

The range of the film parameter values for the four lubrication regimes is as follows [9]:

1. Hydrodynamic lubrication $5 \leq \Lambda < 100$

2. Elastohydrodynamic lubrication $3 \leq \Lambda < 10$

3. Partial lubrication $1 \leq \Lambda < 5$

4. Boundary lubrication $\Lambda < 1$

Thus the combination of high load and low surface speed in the pin-joint results in the condition of boundary lubrication between the contacting surfaces.

Most of the failure modes associated with pin joints are caused by high contact stress and wear. This paper will not concentrate on the seal design for improved lubrication, which is also of great concern, but rather the pin joint will be redesigned such that the contact stress between the pin and the bushing is reduced.

2.2.3   Galling

A failure mode often encountered in such bearings is galling. The term galling has many different definitions. The American Society of Testing and Materials has defined

galling as "a form of surface damage arising between sliding solids, distinguished by macroscopic, usually localized, roughening and creation of protrusions above the original surface. It often includes plastic flow, or material transfer, or both." Budinski defines galling as "damage to one or both members in a solid-to-solid sliding system caused by macroscopic plastic deformation of the apparent area of contact, leading to the formation of surface excrescences that interfere with sliding" [4].

The mechanism of galling involves local adhesion, plastic deformation and ductile rupture of adhesive junctions which have formed in the contact region [23]. Galling may also be caused by micro-welding or delamination wear. In micro-welding, as the title implies, the material on the surface of the pin and the bushing weld together, caused by the high temperatures resulting from the contact of the surfaces. Through delamination wear, the small wear particles caused by the rubbing of the material act as stress risers which result in the formation of cracks on the pin and the bushing.

Galling is characterized as a type of adhesion-initiated catastrophic wear (AICW). The low-energy types of AICW include seizure and scoring [15]. Scoring is associated with scratches across the rubbing surfaces. The high-energy types of AICW include scuffing and galling. Scuffing is mainly associated with high load, high speed, lubricated conditions, whereas galling is associated with dry or poorly lubricated conditions. AICW is characterized by a concentration of normal load and plastic flow on the surfaces of a friction pair within a small area. This results in the formation of protrusions and widening grooves on the surfaces and in sharp increases of surface roughness and wear rate. According to Markov and Kelly, galling occurs when there is a transfer of material from a softer surface onto a harder surface [15]. The subsequent layers of transferred metal are smeared over the earlier ones. The layers transferred during galling have small thickness, and have homogenous structure and hardness. Markov has thus hypothesized that galling results from concentration of energy so intense that metal flows as amorphous material without hardening (dislocation deformation). The deformed metal hardens only after interruption of the material flow. Thus galling scars are shallow and not expanded.

Another theory associated with galling is proposed by Bhansali and Miller, who

state that the tendency to gall is related to the stacking fault energy [2]. Materials with low stacking fault energy tend to strain harden rapidly and thus show the highest resistance to galling. Stacking faults hinder dislocation cross-slip, and high stacking fault energy indicates a low number of impeding stacking faults. Materials with high stacking fault energies, such as nickel and aluminum, are known to have high galling tendency.

Some of the factors that affect galling include the contact pressure between the surfaces, relative surface velocity, lubrication, surface finish, and material properties. It has been recommended that to improve galling, the contact pressure should be reduced and the surfaces be lubricated sufficiently [5]. The risk of galling is increased for surfaces with similar chemical compositions and mechanical properties. Elevated temperatures, metallurgically clean surfaces, and hard particles trapped between the sliding surfaces also increase the tendency to gall [13]. Polished surfaces also have been known to gall more easily than rough ones. This can be attributed to the fact that polished surfaces present a larger area of deformation than a rough surface. Surface waviness also contributes to the galling conditions. Brittle surfaces also have been found to gall less than ductile surfaces [3]. Other factors that reduce galling are high hardness and rapid work hardening [23]. Hardness can be increased by either applying a hard coating or surface treating the material. One type of coating which has been proven to be effective against galling are the carbon-based coatings (DLC and IonSlip), which lower the coefficient of friction [23]. Thermal oxidation also provides good protection, but has higher friction coefficient than the previously mentioned coatings. TiN is effective at lower load range, but fails to protect at higher loads.

The onset of galling can be detected by a sudden increase in friction [23]. The surface roughness of the contact area can also be analyzed in order to determine whether galling has occurred. The severity of galling can be quantified by the roughness and the number and depth of the scratches formed on the surface [1]. Another characteristic of galling is the presence of long grooves on the surface of the contact region (Figure 2-1).
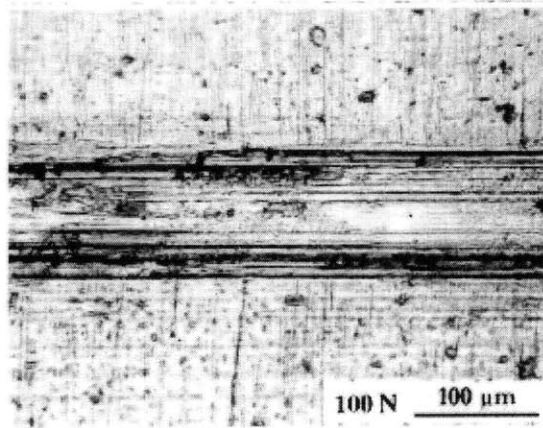
Figure 2-1: Galled Surface

Chapter 3

Redesign of the Pin Joint Through Contact Stress Analysis

The goal of the redesigned pin joint is to increase its service life. As discussed in the previous section, this can be achieved by decreasing the maximum contact pressure in the the pin joint for a given applied load. Due to geometric constraints, the size of the pin joint can not be increased. Thus it is necessary to redesign the pin joint elements in order to achieve this goal.

The contact stress can be analyzed through either the Hertzian model of contact, or numerically through finite element analysis. But before analyzing the contact stress, it is necessary to conduct a dimensional analysis in order to understand how the stress scales with different parameters.

3.1 Dimensional Analysis of the Contact Stress

Dimensional analysis can be used to simplify expressions for the relationship between important mechanical properties. It can reduce the amount of experimentation needed in order to have a complete description of the mechanical phenomena.

A unit of dimension is used to quantify physical properties of a system. The fundamental dimensions include mass, length, time, temperature, and electric current, which are independent of each other. By using the Π-theorem, the relationship be-

tween n physical variables can be reduced to a dimensionless relationship among $n - r$ dimensionless variables so that

$$\Pi_1 = f(\Pi_2, \Pi_3, ...\Pi_{n-r}) \tag{3.1}$$

where the Πs are independent of each other. The procedure for determining the Πs is as follows [7]

1. Determine the number of fundamental dimensions d that appear in the equations

2. Choose r independent variables that contain all the fundamental dimensions

3. For the remaining $n - r$ variables, form a Π by finding the product of that variable and the selected variables that is dimensionless

The stress σ is measured in terms of $\left[\frac{M}{LT^2}\right]$. Its functional form can be written as

$$\sigma = f(F, E, l, D, d, \nu) \tag{3.2}$$

where F is the force, E is the modulus of elasticity, L is the length of the pin, D is the diameter of the bushing, d is the diameter of the pin, and ν is the poisson ratio. The dimensions of these variables are as follows:

$$F = \left[\frac{ML}{T^2}\right] \tag{3.3}$$

$$E = \left[\frac{M}{LT^2}\right] \tag{3.4}$$

$$D = d = l = [L] \tag{3.5}$$

$$\nu = \text{dimensionless} \tag{3.6}$$

Choosing F and l as the independent variables, Π_1 can be determined

$$\Pi_1 = \sigma F^a l^b = \left[\left(\frac{M}{LT^2}\right)\left(\frac{ML}{T^2}\right)^a (L)^b\right] = \left[M^{(1+a)} L^{(a+b-1)} T^{(-2(a+1))}\right] = \left[M^0 L^0 T^0\right] \tag{3.7}$$

24

$$a + 1 = 0 \tag{3.8}$$

$$a + b - 1 = 0 \tag{3.9}$$

$$2(a + 1) = 0 \tag{3.10}$$

which results in $a = -1$ and $b = 2$, and thus $\Pi_1 = \frac{\sigma}{(F/l^2)}$ or $\frac{\sigma}{(F/Dl)}$. The rest of the Πs can be determined in a similar manner:

$$\Pi_2 = EF^a l^b = \left[M^{(1+a)} L^{(a+b-1)} T^{(-2(a+1))} \right] = \frac{E}{(F/Dl)} \tag{3.11}$$

$$\Pi_3 = DF^a l^b = \left[M^{(a)} L^{(a+b+1)} T^{(2a)} \right] \tag{3.12}$$

which results in $a = 0$ and $b = -1$, and thus $\Pi_3 = \frac{D}{l}$. Similarly $\Pi_4 = dF^a l^b = \frac{d}{l}$.

Thus the nondimensional parameters as determined through the Π-theorem are

$$\frac{\sigma}{(F/Dl)} = f\left(\frac{E}{(F/Dl)}, \left(\frac{D}{l}\right), \left(\frac{d}{l}\right), \nu \right) \tag{3.13}$$

The significance of this result is that the contact stress in the pin joint can be scaled by keeping the dimensionless parameters constant. For example, if the modulus of elasticity of the pin joint material is increased by a factor 10 with the geometry remaining the same, the force also needs to be raised by a factor of 10 in order to have a properly scaled experiment.

3.2   Hertz Model of Contact Stress

According to Hertz, two non-conformal and elastic bodies in contact will have a contact area elliptical in shape. Each body can be modelled as an elastic-half space. Two important conditions must be met for Hertz theory: the characteristic length of the contact area must be small compared with (1) the dimensions of each body, and (2) the relative radii of the curvature of the surfaces [14]. Friction is also neglected in Hertz contact model, so that only normal pressure is transmitted between the bodies. In order to meet these conditions, the elastic bodies must be non-conforming. For

25

the case of a straight pin and straight bushing, the contact area would be rectangular in shape and the bodies would be considered conformal. But the bushing has two lobes on its inside surface, which result in elliptical area of contact. In order to determine whether the contact between the pin and the bushing is Hertzian, the model is analyzed (see Appendix B for detailed analysis of the Hertzian model) and compared numerically to the results from finite element analysis.

For a total applied load of 100,000 lbf (50,000 lbf per lobe), the maximum contact pressure P_0 from the Hertzian analysis is 1024 MPa. The length of the major axis of the contact ellipse a is 30 mm and the length of the minor axis b is 3.5 mm. The resulting deformation δ of the two bodies is 0.12 mm. For a total applied load of 10,000 lbf:

P_0= 475 MPa; a= 14 mm; b= 1.6 mm; δ= 0.025 mm.

The Hertzian model can be refined by adding additional parameters. As mentioned above, the only relevant external conditions for a pure Hertzian contact is the normal load between the contacting surfaces. In order to add traction to the model, it is required to make assumptions about the frictional behavior of the interface (such as the friction coefficient). The sliding speed and slip distributions become important factors in the model. Traction increases the maximum shear stress and also brings it closer to the surface [22]. The addition of plasticity to the model requires flow properties of the material, which lead to the calculation of the magnitude and location of plastic strain and plastic heat generation. Plastic strain causes redistribution of elastic stress field and leaves residual stresses after load is removed [22]. The roughness of surface in the model requires geometric measurement of the root-mean-square roughness, the spacing between asperities, and the typical asperity slope. Micro-stresses and local temperature rises near the asperities become crucial in this model.

3.3 Finite Element Analysis of the Pin Joint

The pin and the bushing are modelled using the SDRC-IDEAS finite element package. Contact elements are incorporated on the surface of the pin and the bushing and

symmetric loading and boundary conditions are applied in the model. The lobe was also added to the model for the purpose of comparison to the Hertzian analysis.

3.3.1 Finite Element Procedure

In order to understand the validity and accuracy of the model, a brief summary of the contact solution method used by the SDRC solver is presented [18]. The algorithm used by the contact solver involves kinematic equations and equilibrium equations, which are then assembled into a matrix. The kinematic equations describe the relative motion of the two contacting surfaces. The penetration of the hitting point into the target point is

$$p = p_0 + (u_H - u_T) \cdot n \tag{3.14}$$

where

p_0 is the initial penetration determined by the geometry

u_H is the motion of the hitting point

u_T is the motion of the target point

The contact constraints are imposed at the integration points on the finite element faces of the hitting contact region. The constraints are given by

- $p \leq 0$, which imposes that the penetration of the hitting surface into the target surface can't be greater than zero (thus the surfaces can't interpenetrate)

- $t_n = -n \cdot t \geq 0$, where t_n is the contact pressure defined as the negative of the normal component of the surface traction. This equation states that the contact pressure can't be less than zero (must have compressive normal traction)

- $t_n p = 0$ imposes that p=0 if $t_n \geq 0$ and t_n=0 if $p \leq 0$

The finite element method discretizes the contacting bodies into elements. The contact constraints are imposed at nodal points for node-to-node gap elements and node-to-ground gap elements. The penetration in terms of finite element degrees of freedom is given by

27

$$p = p_0 + (\sum_{i=1}^{nH} N_H^i u_H^i - \sum_{j=1}^{nT} N_T^j u_T^j) \cdot n \tag{3.15}$$

where

N_H^i are the interpolation functions for the i nodes on the hitting face

N_T^j are the interpolating functions for the j nodes on the target face

u_H^i and u_T^j are the nodal displacements on the hitting and target faces.

The interpolation functions depend on the locations of the hitting and target points. The equation can be written as

$$p = p_0 + [q_0] \begin{pmatrix} u_H \\ u_T \end{pmatrix} \tag{3.16}$$

where u is the contact element nodal displacement and $[q_0]$ is composed of interpolation functions multiplied by the components of the surface normal.

The two methods used to solve this equation are based on the augmented Largrangian procedure. Through this procedure, a penalty stiffness is added, and the contact constraints are satisfied through a series of contact traction iterations. For the frictionless problem modelled, the augmented Lagrangian potential function is

$$\Pi = \frac{1}{2} U^T [K] U - U^T F + T_n{}^T ([Q_n]U + P_0 + \frac{1}{2}([Q_n]U + P_0)^T [\epsilon_n]([Q_n]U + P_0)) \tag{3.17}$$

where T_n is the vector of unknown normal traction at the contact points and $[\epsilon_n]$ is a diagonal matrix of normal penalty numbers. Taking the derivative of the potential functions with respect to displacement and setting it equal to zero with constant vector of normal tractions produces

$$([K] + [Q_n]^T [\epsilon_n][Q_n])U = F - [Q_n]^T (T_n + [\epsilon_n]P_0) \tag{3.18}$$

where $[Q_n]^T [\epsilon_n][Q_n]$ is a penalty stiffness and $[Q_n]^T (T_n + [\epsilon_n]P_0)$ is an additional force term resulting from the contact pressure and any initial non-zero penetration. The contact pressure is iteratively updated for each contact element to enforce the zero

28

penetration constraint condition to within a specified tolerance. The iterative update formula for the normal contact traction is given by

$$t_H^i = t_H^{i-1} + \epsilon_n p \tag{3.19}$$

where p is the current value of penetration at the point and ϵ_n is the normal penalty number.

The steps for the solution procedure include:

1. Form contact elements from user input of the global search parameters and the definition of the contact regions and pairs

2. Compute stiffness for all elements including penalty stiffness for contact elements

3. Compute loads for the current load case

4. Begin contact outer loop iteration. Determine contact elements status, depending on penetration and contact tractions

5. Assemble contact stiffness for active contact elements into the global stiffness matrix

6. Begin contact inner loop iteration

7. Update contact tractions and compute contact forces

8. Check traction convergence. If tractions have not converged, loop back to step six. If tractions have converged, loop back to step four. If tractions have converged and contact status hasn't changed, proceed with the next load case.

3.3.2 Model Setup

The boundary conditions incorporated in the model include the applied load on the pin and the displacement restraint on the surfaces of the pin joint. The load is modelled as uniform pressure on the surface of the pin, applied in the vertical direction.
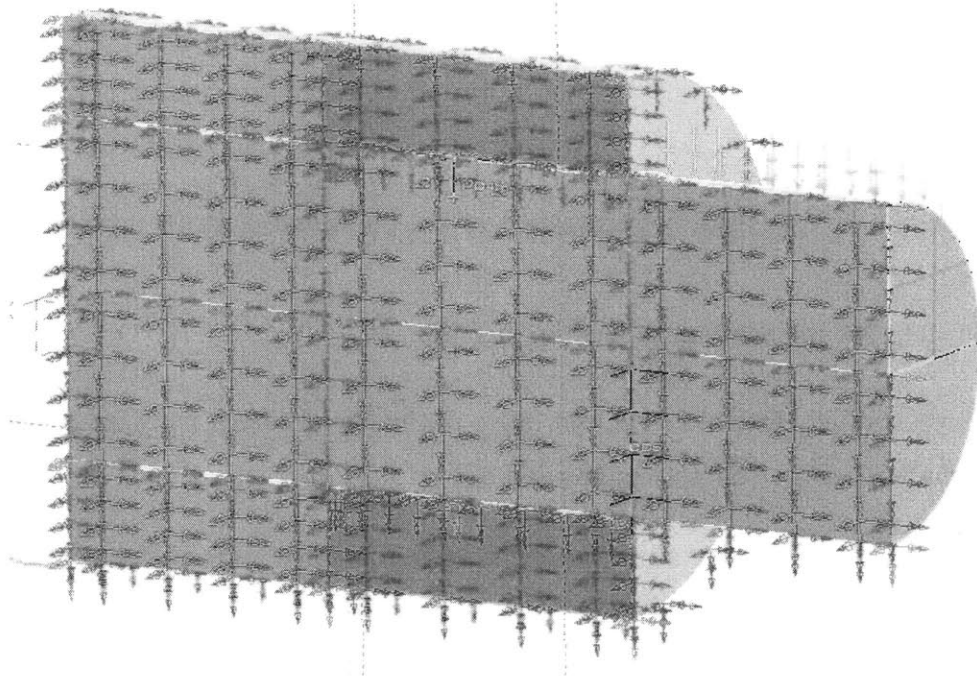
Figure 3-1: Boundary Conditions

There are two planes of symmetry for the pin joint model. One plane of symmetry is at the mid-plane of the pin joint, and the second is through the diameter of the pin joint. The pin joint is restrained from displacement in the axial direction and from out-of-plane rotation at its end (corresponding to the plane of symmetry at the midpoint). The same concept is used at the surface corresponding to the diametrical plane of symmetry, where the displacement normal to the plane and the rotation out of plane are set to zero (see Figure 3-1).

The outer surface of the bushing is restrained to zero displacement in all directions (in service, the bushing is press-fit into a housing, and thus the outer surface is restrained). The contact elements are formed between the surface on the inner diameter of the bushing and the outer surface of the pin.

The meshing incorporates 3D tetrahedral elements within the solid body. There are a total of 25,000 elements created for the pin joint. The critical areas of contact have a finer mesh, with element length of 4 mm. The non-critical areas of the pin

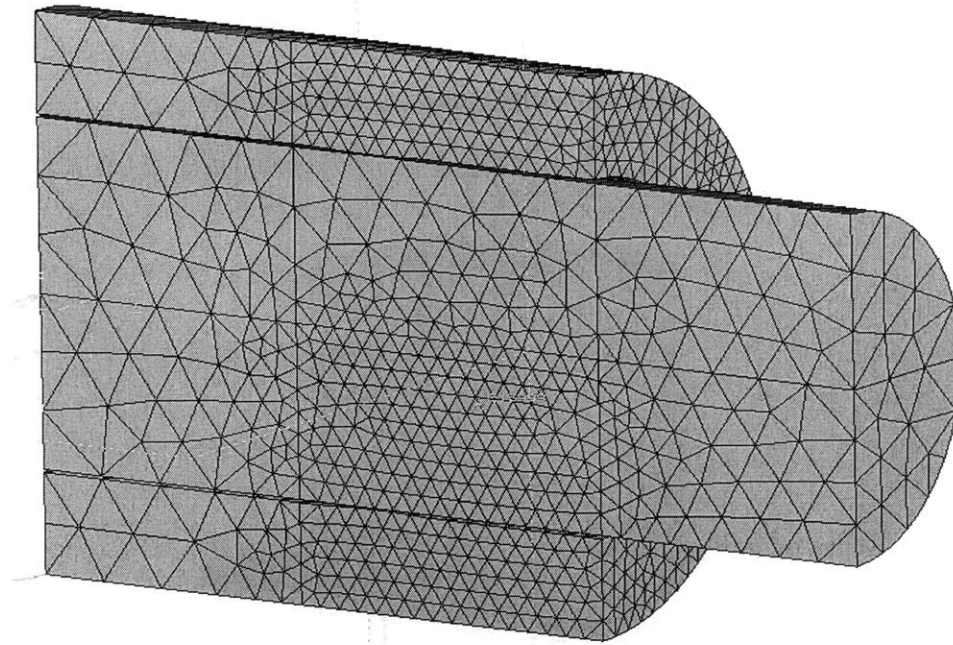joint are meshed with 10 mm long elements (see Figure 3-2).

Figure 3-2: FEM Mesh

3.3.3 Finite Element Results

With a normal load of 10,000 lbf, the maximum contact pressure in the lobe region is 756 MPa, which is 60% greater than the value calculated through the Hertzian model. The discrepancy between the finite element result and the Hertzian result reduces the validity of applying the pure Hertzian contact model to the pin joint. As mentioned earlier, the Hertzian model assumes that the length of the contact region is small compared to the relative radii of curvature. At 10,000 lbf of load, the length of contact a is 0.014 m, compared to 0.2 m for R", and 4.9 m for R'. The ratio between a and and R" is not small enough for the assumption to hold.
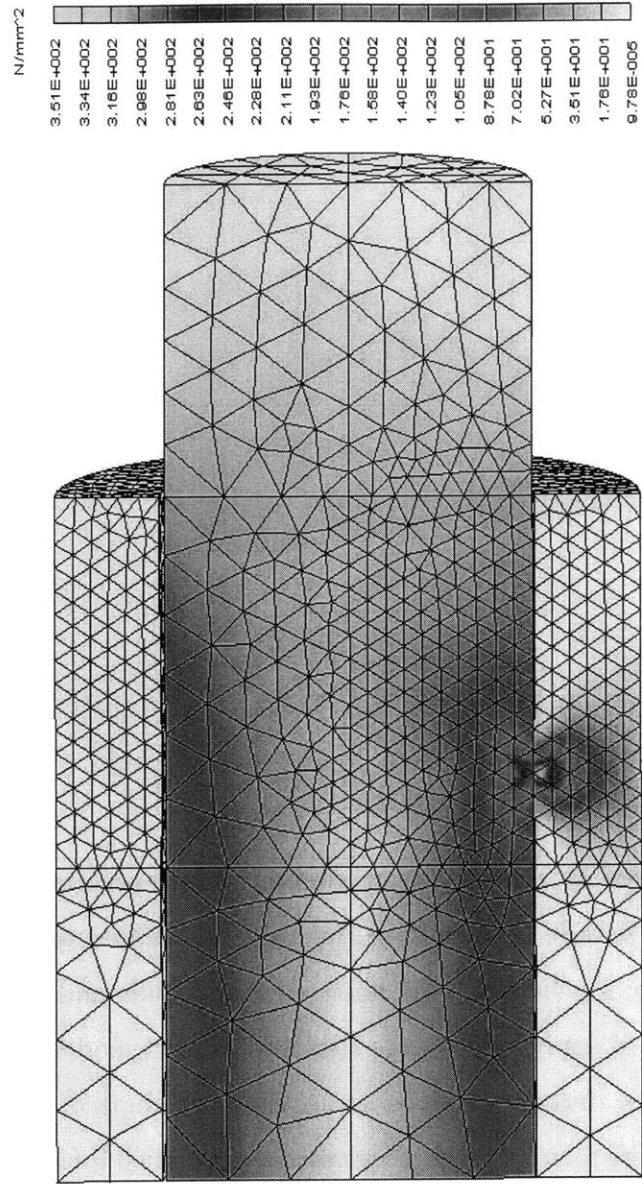
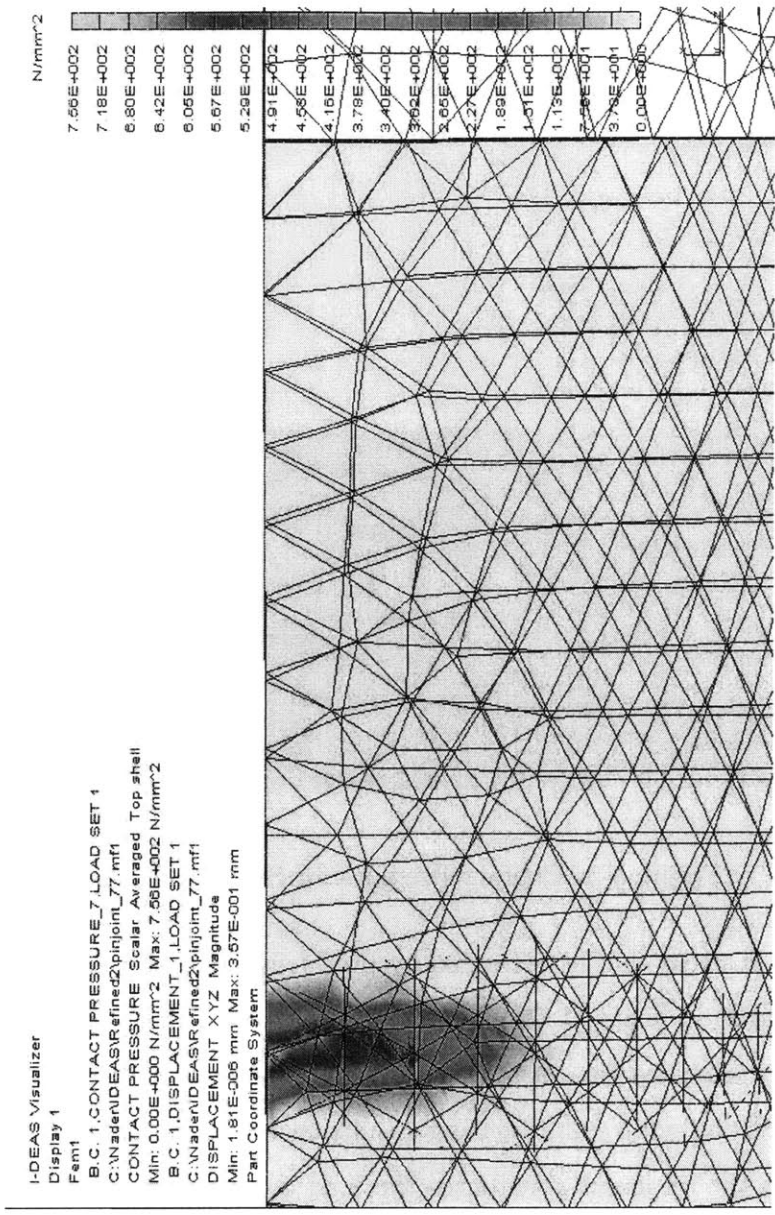Figure 3-3: Pin joint finite element model

Figure 3-4: Contact Pressure of Lobed Pin joint (Normal load 10,000 lbf)

3.4   Redesign of the Pin Joint

One novel concept that can be applied to the design is to stress-relieve the critical contact area. For a straight bushing with no lobe, the maximum contact pressure is located at the region where the inside edge of the bushing contacts the outer surface of the pin. This is verified through finite element analysis as shown below (SDRC I-DEAS package used).
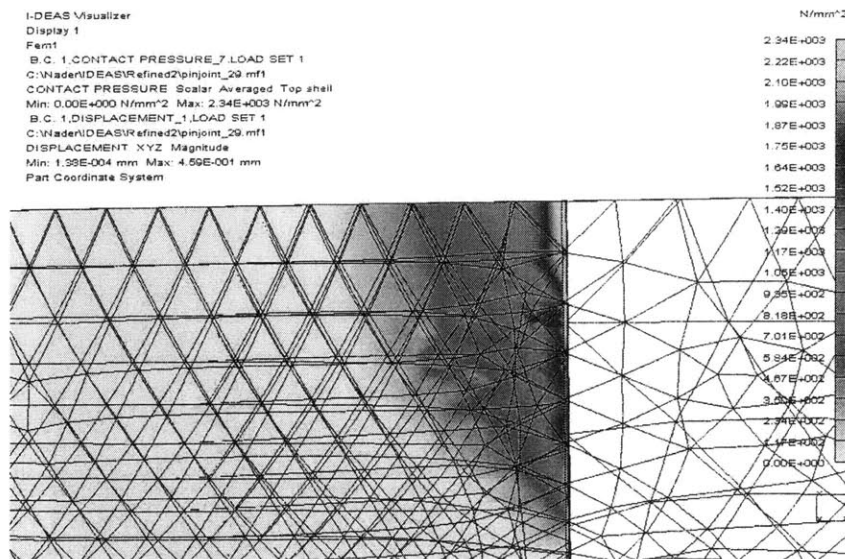
Figure 3-5: Contact Pressure for Straight Bushing

The contact stress can be decreased by producing an undercut on the face of the bushing as shown in Figure 3-6. The undercut creates a stress-relief for the edge of the bushing by allowing the bushing-end to deflect under the load. The decrease in the stiffness at the end of the bushing results in lower contact pressure. Also the lip created by the undercut distributes the load over the area of the lip. Thus the deeper the undercut is into the bushing, the greater the area over which the load is distributed, and thus the lower the maximum contact pressure. There are three undercut parameters that affect the amount of stress relief: the depth of the cut (D1), the width of the cut (D2), and the thickness of the lip (D3) (see Figure 3-6). Figure 3-9 shows the trend of the maximum pressure versus the depth of the undercut.

34

The maximum contact pressure calculated for the uncut pin joint is 2340 MPa. The contact pressure tends to level off as the depth of the undercut is increased. The larger the width of the cut (D2), the higher the stress relief in the pin joint and the lower the maximum contact pressure. The thickness of the lip also has significant effect on the stress relief, and has an optimum value for lowering the contact stress (see figure 3-10). In order to achieve the highest reduction in contact stress, the design is optimized over the three parameters.
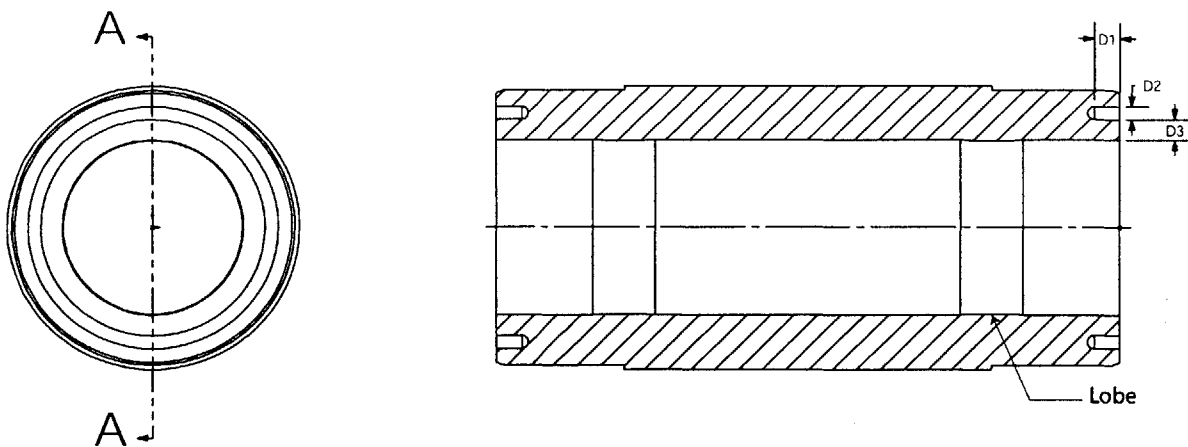
Figure 3-6: Undercut Bushing

Through iterations on finite element analysis, the optimized undercut design was determined to be at D1=20 mm , D2=8 mm , and D3=9.3 mm. The maximum contact pressure for this case is 543 MPa, which is 23% of that computed for the straight bushing.

One of the concerns with creating an undercut is the introduction of higher stress around the lobe of the cut. The Von Misses stress associated with the undercut was computed from the finite element model, and the results comparing the cut and the uncut bushing showed no increase in the maximum stress.

I-DEAS Visualizer   N/mm^2
Display 1
Fem1   5.43E+002
 B.C. 1,CONTACT PRESSURE_7,LOAD SET 1   5.16E+002
C:\Nader\IDEAS\Refined2\pinjoint_50.mf1
CONTACT PRESSURE Scalar Averaged Top shell   4.89E+002
Min: 0.00E+000 N/mm^2 Max: 5.43E+002 N/mm^2   4.62E+002
 B.C. 1,DISPLACEMENT_1,LOAD SET 1   4.35E+002
C:\Nader\IDEAS\Refined2\pinjoint_50.mf1
DISPLACEMENT XYZ Magnitude   4.08E+002
Min: 5.73E-004 mm Max: 6.95E-001 mm
Part Coordinate System   3.80E+002

3.53E+002

3.26E+002

2.99E+002

2.72E+002

2.45E+002

2.17E+002

1.90E+002

1.63E+002

1.36E+002

1.09E+002

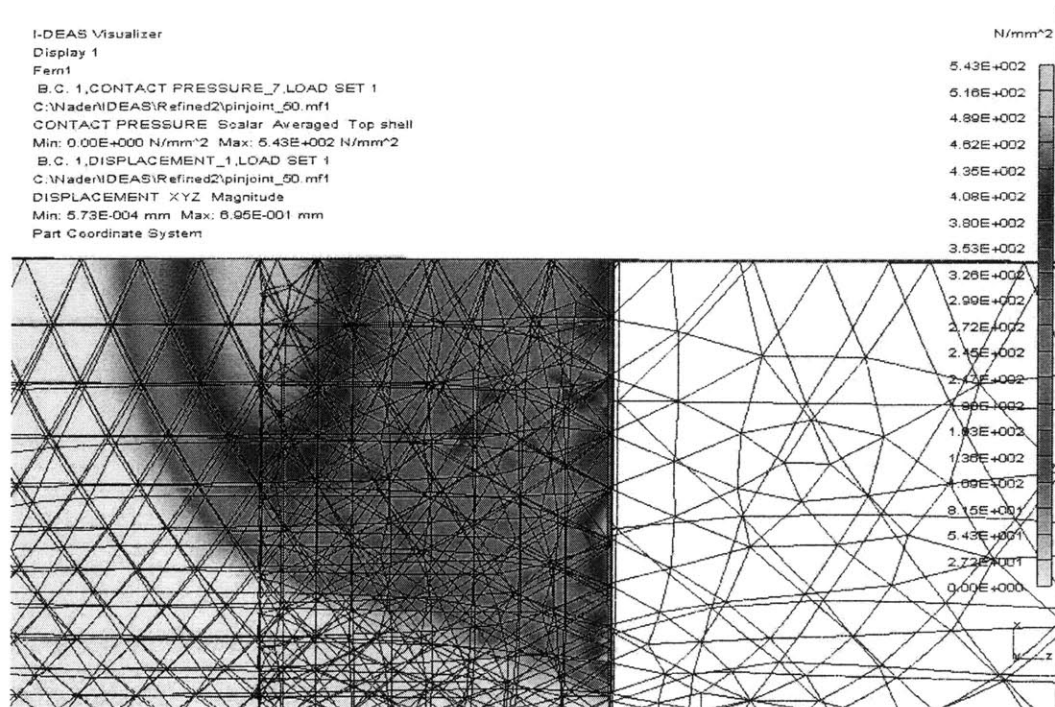8.15E+001

5.43E+001

2.72E+001

0.00E+000

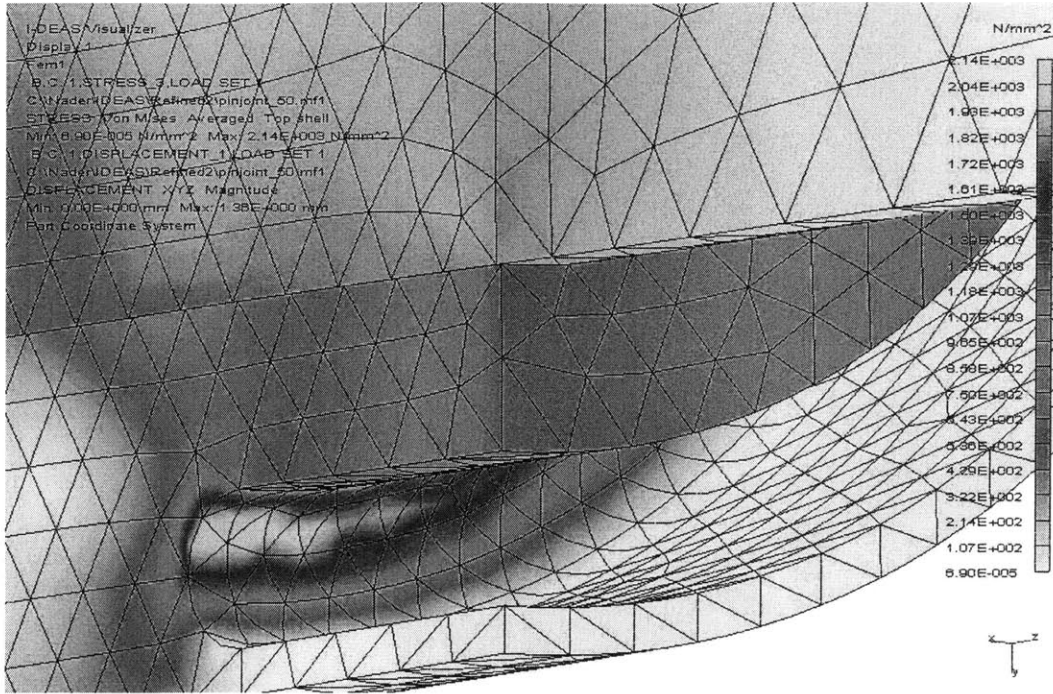Figure 3-7: Contact Stress for Optimum Cut Bushing

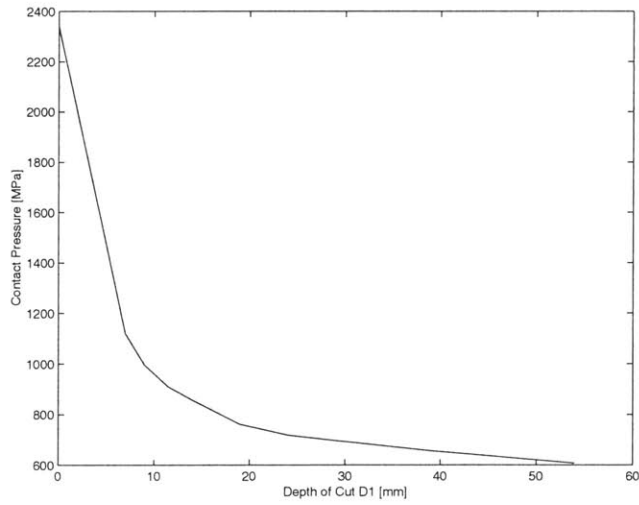Figure 3-8: Von Mises Stress for Optimum Cut Bushing

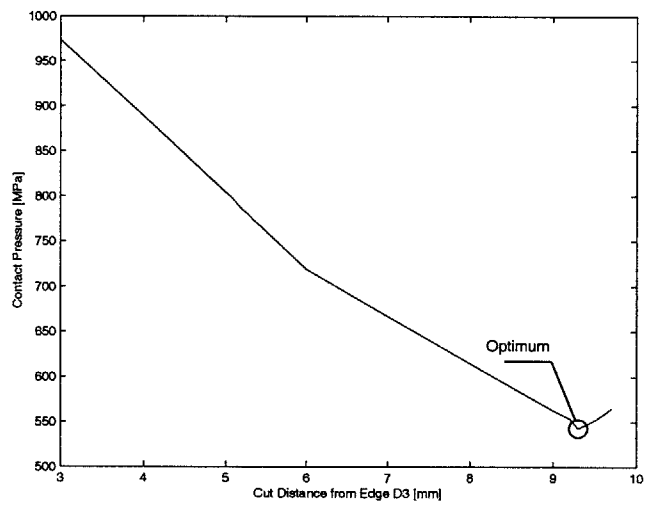Figure 3-9: Contact Pressure vs. Depth of Cut (D1=20 mm, D2=8 mm)

Figure 3-10: Contact Pressure vs. Cut Distance from the Edge

Chapter 4

Pin Joint Test and Results

In order to compare the operational life of the undercut pin joint to the uncut lobed design, testing was conducted through the use of a pin joint test machine developed as part of this project (see Appendix A). The test machine can apply a maximum load of 100,000 lbf through the use of 8 bolts, and is able to oscillate the pin through 25 degrees of rotation at a rotational speed of 2.5 radians per second (close to its normal operating speed). The machine can not exactly replicate the true operating conditions since it only applies a static load, but it is still very useful for comparing the operational life for the different pin joint designs.

The parameters monitored by the test machine include the normal load measurements from the two load cells placed underneath the pin supports, the torque to rotate the bushing which is calculated from the measurements of the third load cell that is placed in the support armature, and the temperature inside the pin measured by the thermocouple. The load measurements can be used to estimate the friction force in the pin joint, and the temperature measurement can be used to estimate the rise in temperature of the lubricant. Unfortunately there was no direct access for the thermocouples to measure the temperature in the contact zone.

The test is conducted in multiple phases, each phase lasting for 10 minutes. The pin joint is loaded to 8,000 lbf in the initial phase, and the applied load is increased by 4,000 lbf before the start of each successive phase (see figure 4-2). The machine is stopped between each phase and the bolts are loosened to release the load. With
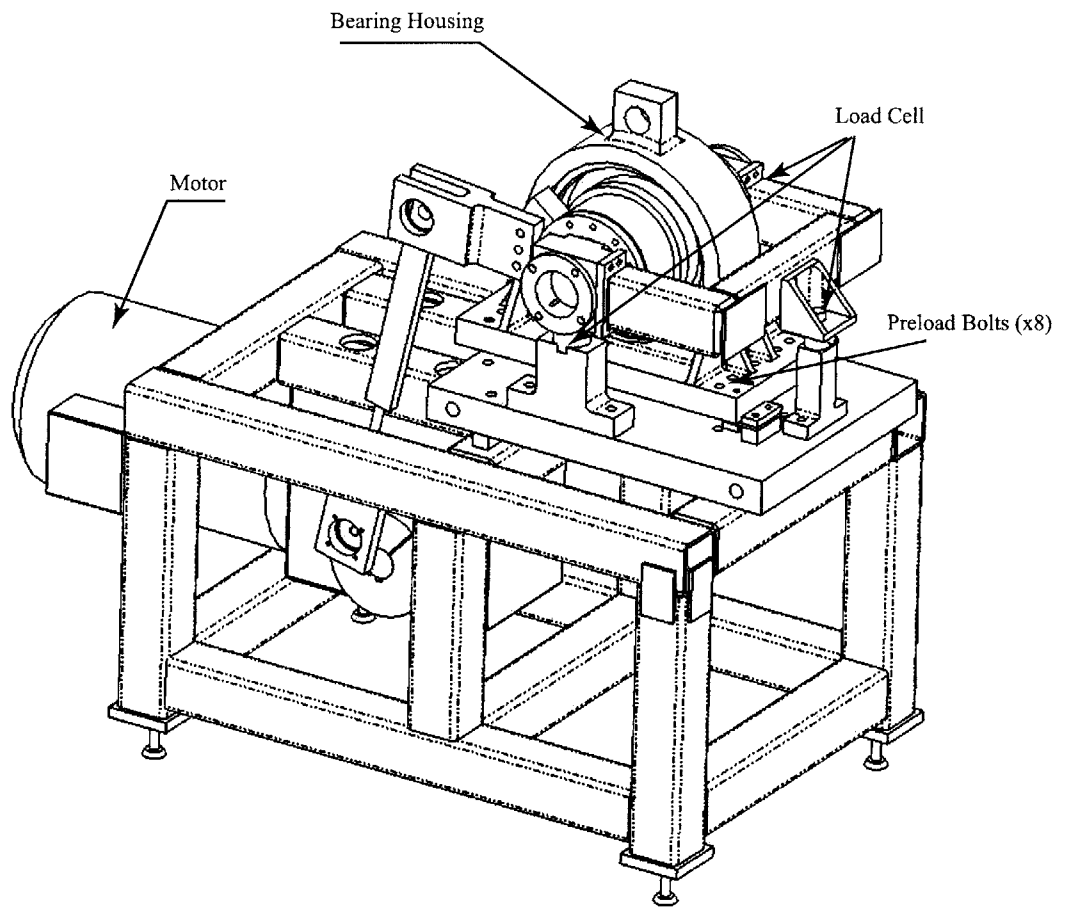
Figure 4-1: Test Stand

the use of 6 springs placed underneath the bearing housing, the weight of the bearing and the bearing-housing is supported and thus there is no normal load on the pin joint. The machine is run for 30 seconds without the normal load, thus replenishing the contact zone with the lubricant before the start of the next phase.

The test is run until failure occurs in the pin joint. The failure involves a significant increase in vibration and noise from the pin joint, a jump in the torque measurement, and an increase in temperature.
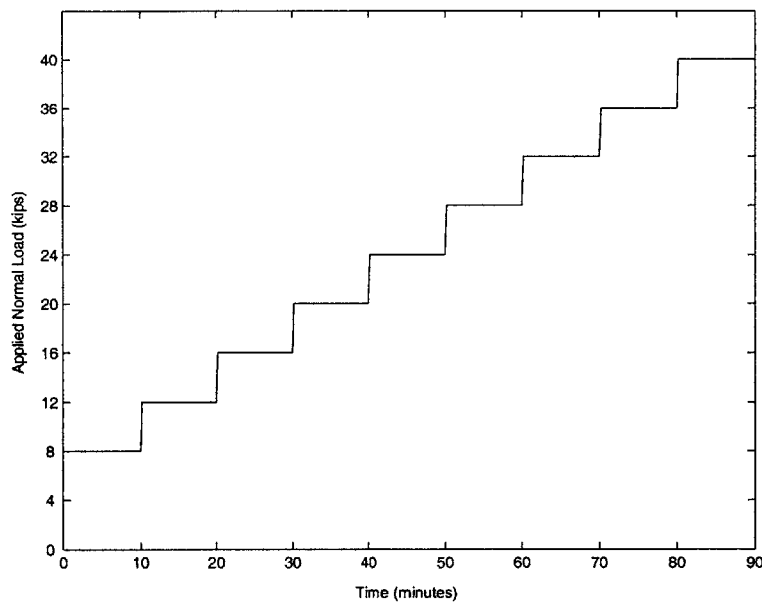
Figure 4-2: Applied Normal Load Profile

4.1 Initial Test Results

The test runs conducted with the uncut lobed bushings failed at the applied normal load of 24,000 lbf and 28,000 lbf. The first test lasted nine minutes into the sixth stage of testing (load of 28 kips). The coefficient of friction increased from 0.15 to above 0.27 at the onset of galling (See Figure 4-4). The temperature of the lubricant also increased from 25 degrees Celsius to 42 degrees.

41

A similar pattern was observed with the other test runs. The second run lasted one minute into the sixth stage of the testing (at 28,000 lbf of load) and the third run failed in the fifth stage (at 24,000 lbf). The coefficient of friction in both cases increased from approximately 0.15 to 0.28 at the onset of galling (See Figure 4-6 and 4-7). The temperature of the lubricant also increased as shown in Figures 4-8 and 4-9.
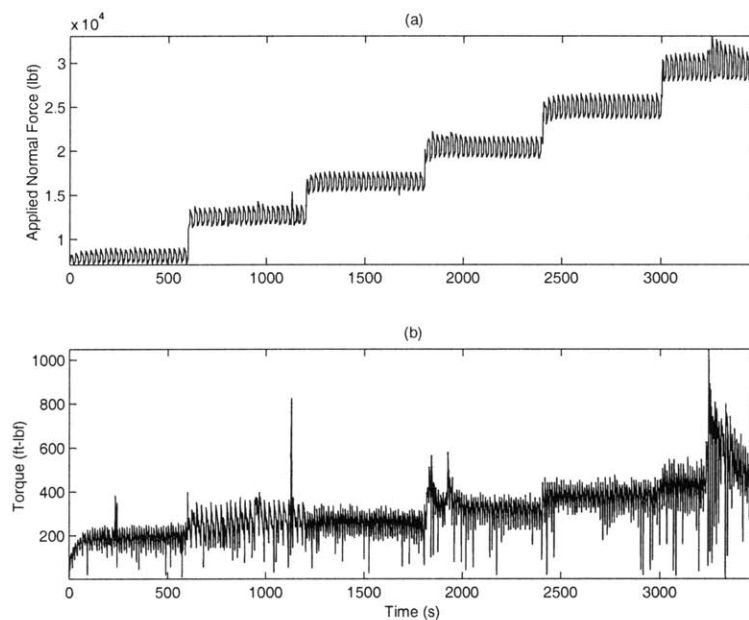
Figure 4-3: Test Results: Uncut-lobed bushing

Testing was also conducted on the undercut bushing with specifications of D1= 10 mm, D2= 5.1 mm, and D3= 7.87 mm. The undercut specifications are not the optima determined through finite element analysis, but rather chosen for ease of manufacturability for an initial test. The test of the undercut bushing showed improvement of the operational life of the pin-joint. The test lasted above 30,000 lbf (see Figure 4-10. The same pattern for the torque and friction coefficient can be seen in this test compared to the uncut pin joint test. Figure 4-11 shows an increase in the torque and coefficient of friction after the failure in the pin joint occurs (coefficient of friction increased from 0.1 to 0.2).
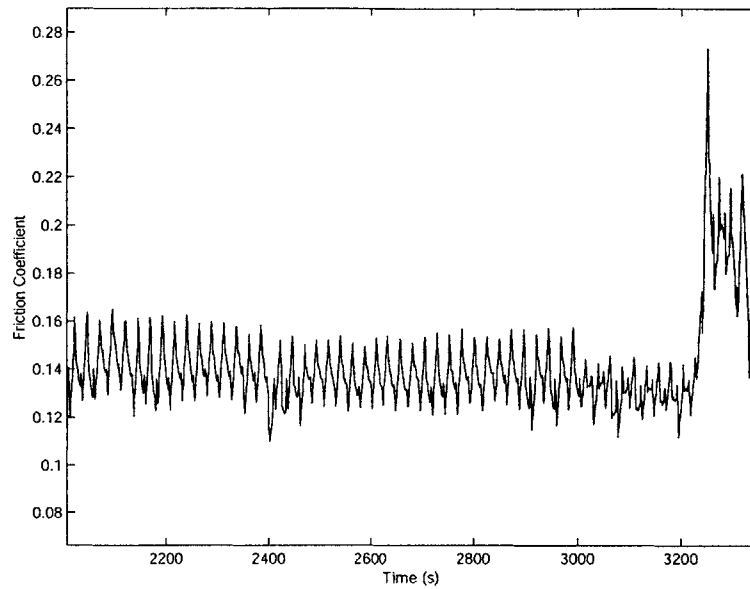
Figure 4-4: Coefficient of Friction for uncut bushing (Run 1)

The increase in time for the test run for the undercut bushing is very promising, but to further validate the test results additional tests with the uncut bushing with the same load profile needs to be conducted.

The surface of the failed bushing shows marks consistent with a galled surface (Fig 4-12). There is transfer of material between the pin and the bushing, and there are long grooves on the area of the contact region. The surface around the grooves is polished, and there is a considerable number of scratch marks around the grooves. The increase in friction and temperature is also consistent with the galling mechanism.
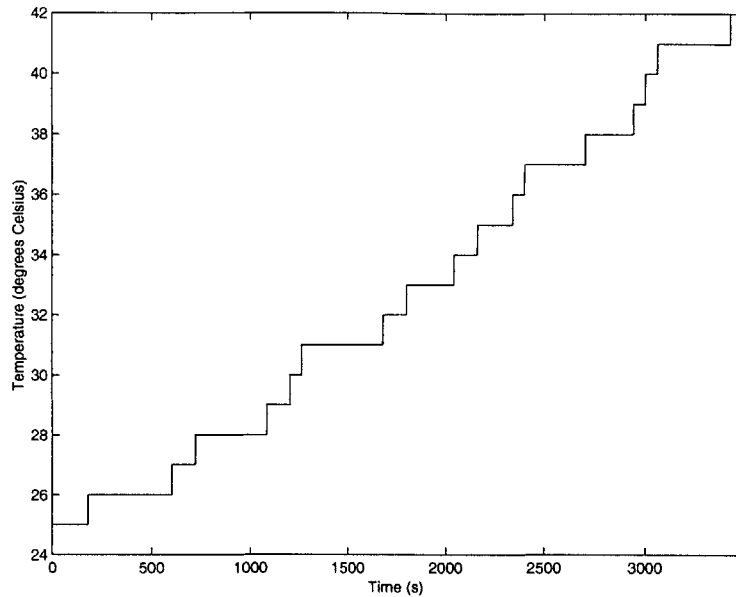
Figure 4-5: Temperature of the Pin (Run 1)

4.2 Future Testing

The initial test results have indicated an increase in the service life of the pin joint through the addition of the undercut in the bushing. In order to have conclusive evidence for this improvement, further tests need to be conducted. One improvement that can be made to the test procedure is the use of an accelerometer to detect the early stages of galling, which results in an increase in the noise and vibration of the pin joint system. Also for improved temperature measurements, the thermocouple needs better access to the contact zone. This can be accomplished by drilling a hole in the pin supports, which would allow the thermocouple to reach the surface of the pin.

Proper sealing also needs to be applied with the undercut bushing. The current seal does not prevent the lubricant from entering the undercut space, and thus the lubricant is squeezed out of the contact zone due to a drop in the lubricant pressure. The lubricant can be sealed out of the undercut region by applying epoxy to the

44

Figure 4-6: Coefficient of friction for uncut bushing (Run 2)

opening of the cut.
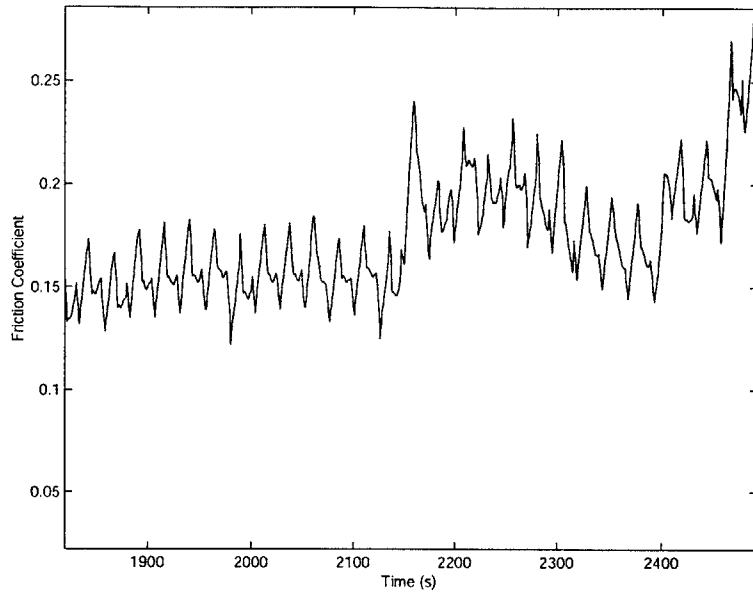
Figure 4-7: Coefficient of friction for uncut bushing (Run 3)
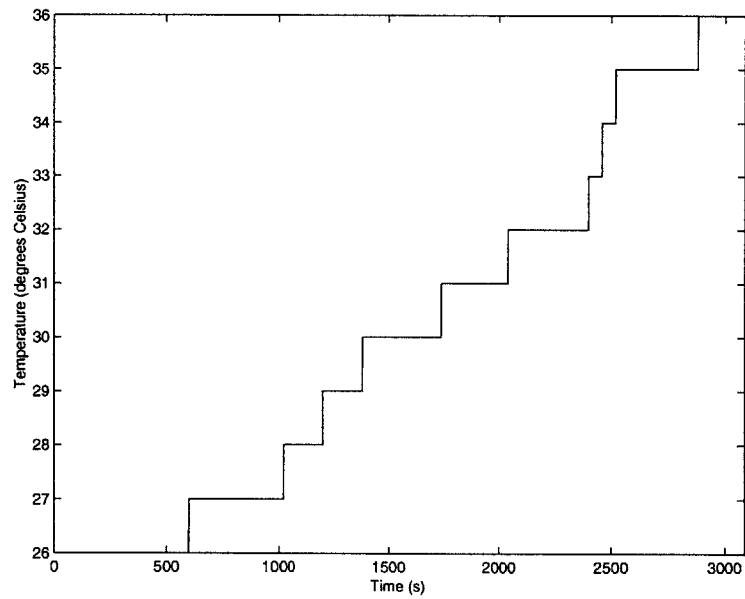
Figure 4-8: Temperature of the Pin (Run 2)
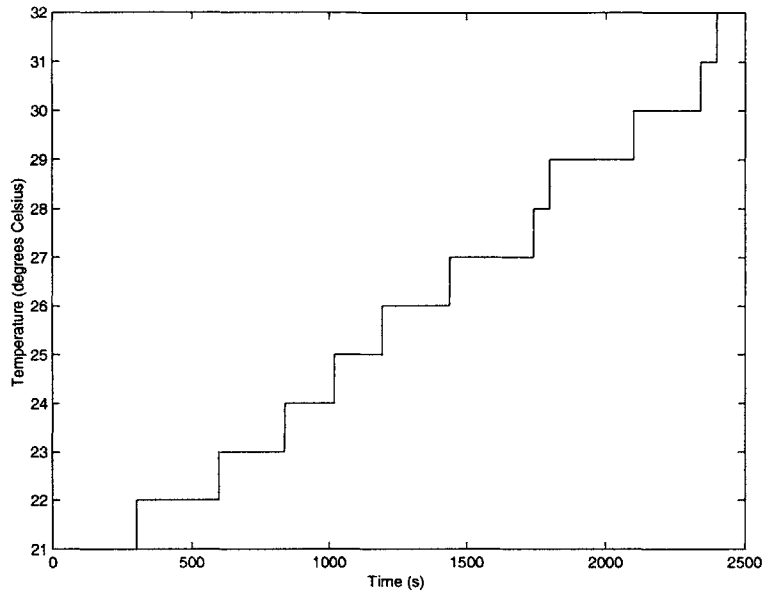
Figure 4-9: Temperature of the Pin (Run 3)
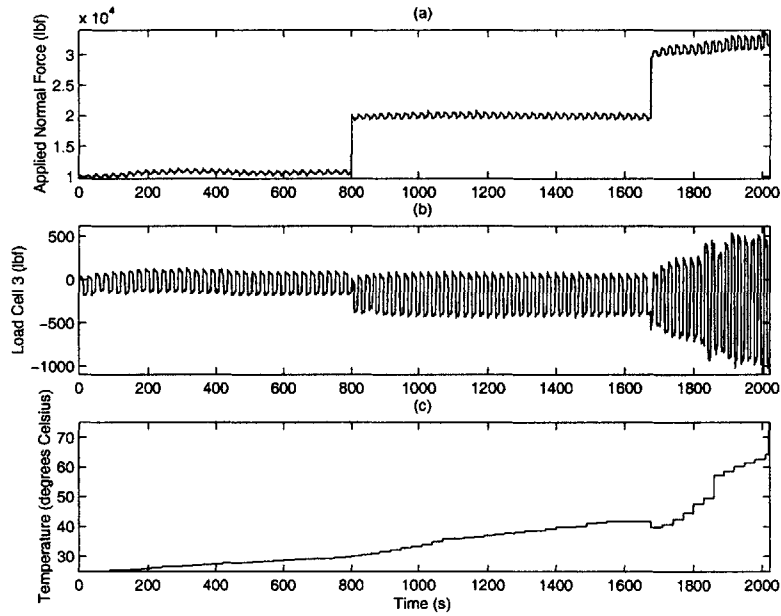
Figure 4-10: Test Results- Undercut Pin Joint

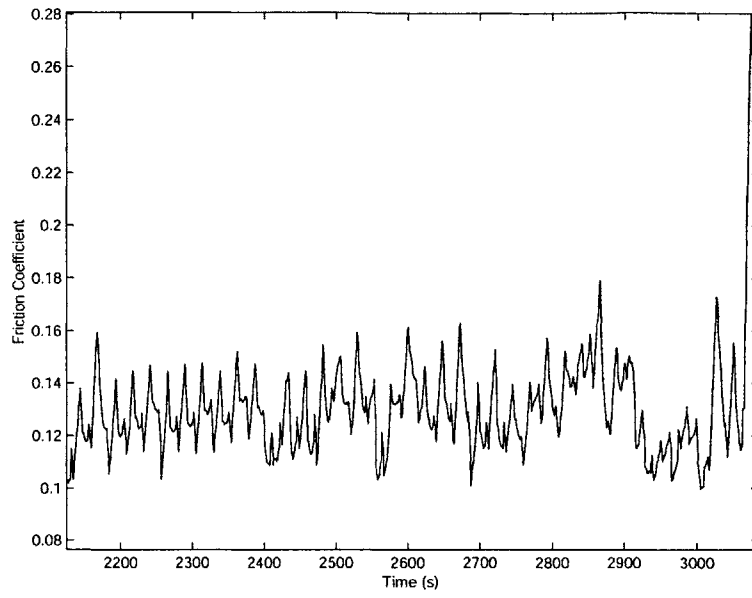47
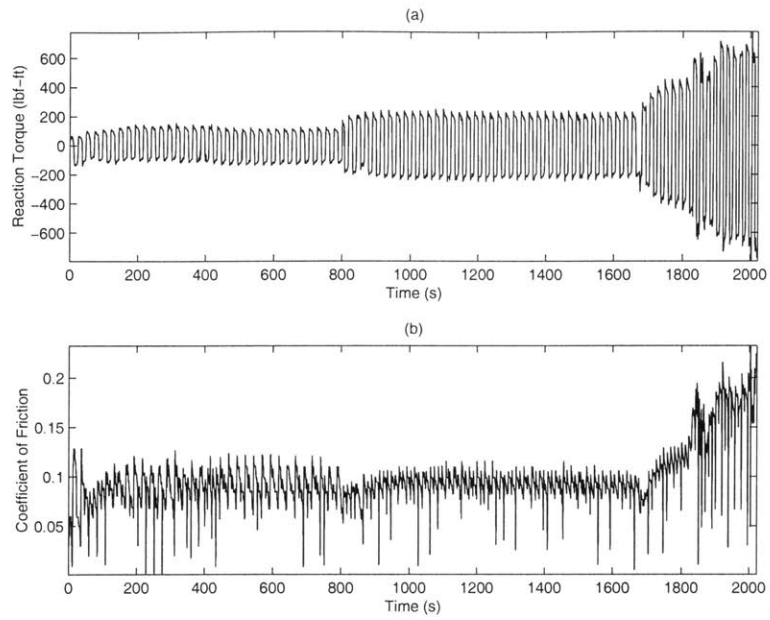
Figure 4-11: Undercut Pin Joint
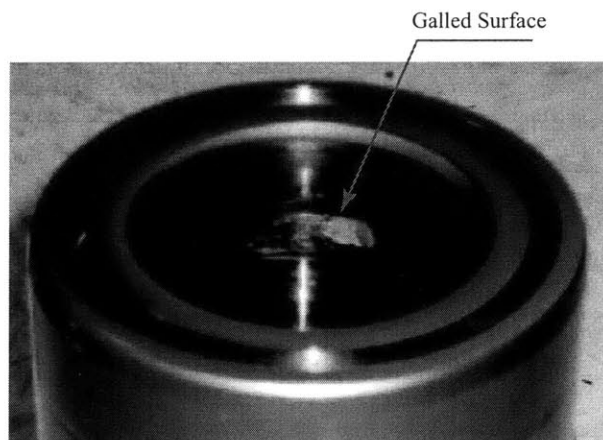
Figure 4-12: Galled Undercut Bushing

Chapter 5

Emission Reabsorption Laser Induced Fluorescence

The behavior of the lubricant in the contact area of the pin-joint is very crucial to its performance and service life. As discussed previously, the lubricant separates the asperities on the surface of the pin and the bushing and thus reduces the wear rate in the pin joint. One reason for the early seizure of the pin joint may be linked to the poor lubrication in the critical contact area in the pin joint. The behavior of the lubricant may be studied by measuring the film thickness separating the pin and the bushing. One lubricant phenomenon which needs to be studied is the "squeeze out" effect resulting from high contact pressure. The surface asperities will come in to contact as the oil is squeezed out of the contact region. The parameters resulting in the oil deprivation, such as the surface velocity and the normal load, can be studied through the optical test. Also the distribution of contact pressure between the pin and the bushing can be inferred from the thickness of the oil film.

The film thickness measurement can be made through an optical technique called Emission Reabsorption Laser Induced Fluorescence (ERLIF), which has been successfully used in the past to measure lubricant thickness in sealing systems [11].

5.1 ERLIF Theory and Background

The photo-excitation of a fluorescent dye is the basis for laser induced fluorescence (LIF). The process of fluorescence occurs in three stages, which are [10]:

1. Excitation of the dye molecules by a photon of energy hv_{ex}, which creates an excited electronic state of S_1'.

2. Partial dissipation of the energy from S_1' to the relaxed state S_1.

3. Fluorescence emission, in which a photon of energy hv_{EM} is emitted and the dye molecule returns to its ground state S_0. Because of energy dissipation, hv_{EM} is lower than hv_{EX} and thus the emitted photon is of a longer wavelength than the excitation photon. The difference between hv_{EX} and hv_{EM} is called Stokes shift, which allows emission photons to be detected by isolating them from the excitation photons.

Fluorescence is a function of the dye characteristics, dye concentration, the excitation light intensity, and the scalar being measured. The total fluorescence emitted by a volume of fluid mixed with a dye can be expressed by:

$$dF = I_e \epsilon(\lambda_{laser}) C \phi dV \tag{5.1}$$

where I_e is the exciting light intensity, $\epsilon(\lambda)$ is the molar absorption coefficient at a given wavelength, C is the dye molar concentration, and ϕ is the quantum efficiency (ratio of the energy emitted to the energy absorbed). Dividing by the area A, the fluorescent intensity normal to the area is

$$dI_f = I_e \epsilon(\lambda_{laser}) C \phi dx \approx I_0 \epsilon(\lambda_{laser}) C \phi t \tag{5.2}$$

where t is the film thickness and I_0 is the exciting light intensity at $x = 0$.

Irregularity of the excitation light intensity can be eliminated by using a ratiometric technique in which the fluorescence intensity is divided by the laser intensity. This can be achieved by using two dyes and computing the ratio of their emissions,

thus eliminating the dependence on the illuminating light intensity. The fluorescence of the first dye contains information about the film thickness and the exciting light intensity. The fluorescence of the second dye also contains the exciting light intensity information, but behaves differently from the first dye with respect to the film thickness. By taking the ratio of the fluorescence of dye 1 and dye 2, the excitation light information cancels and only the desired film thickness information remains.

One phenomenon which occurs when using two dyes is the reabsorption of the fluorescence. Each dye has an absorption spectrum, which is the range of wavelengths over which the excitation of the dye occurs, and an emission spectrum over which the dye fluoresces. Reabsorption occurs when the emission spectrum of one dye overlaps the absorption spectrum of the other. Reabsorption results in a reduction of the fluorescence emission of the first dye. The fluorescent intensity of dye 1 without reabsorption is

$$dI_{f,1} = I_0 \exp\left[-\epsilon(\lambda_{laser})Cx\right] \epsilon_1(\lambda_{laser})C_1\phi_1\eta_1(\lambda)dxd\lambda \qquad (5.3)$$

where ϕ_1 is dye 1 quantum efficiency and $eta_1(\lambda)$ is the relative emission of dye 1 at a given wavelength.

The fluorescent intensity of dye 1 with reabsorption is

$$dI'_{f,1} = I_0 \exp\left[-\epsilon(\lambda_{laser})Cx\right] \epsilon_1(\lambda_{laser})C_1\phi_1\eta_1(\lambda) \exp\left[-\epsilon_2(\lambda)C_2x\right] dxd\lambda \qquad (5.4)$$

The total intensity collected can be found by integrating equation (5.4) over varying film thicknesses and wavelengths. By using a narrow filter, all wavelengths except for the one of interest are filtered out and the total intensity collected can be computed by [10]:

$$I'_{f,1}(t, \lambda_{filter1}) = \frac{I_0\epsilon_1(\lambda_{laser})C_1\phi_1\eta_1(\lambda_{filter1})(1 - \exp[-\epsilon(\lambda_{laser})Ct - \epsilon_2(\lambda_{filter1})C_2t])}{\epsilon(\lambda_{laser})C + \epsilon_2(\lambda_{filter1})C_2}$$

$$(5.5)$$

and the fluorescent intensity of dye 2 is

$$I_{f,2}(t, \lambda_{filter2}, y) = \frac{I_0 \epsilon_2(\lambda_{laser}) C_2 \phi_2 \eta_2(\lambda_{filter2})(1 - \exp[-\epsilon(\lambda_{laser})Ct])}{\epsilon(\lambda_{laser})C} \qquad (5.6)$$

Since the amount of fluorescence absorbed through the layer of dye film is dependent on the film thickness, the reabsorption can be used to determine the film thickness. Taking the ratio of the emissions of the two dyes yields an expression which only depends on the film thickness [10].

$$\frac{I'_{f,1}}{I_{f,2}} = R(t) = \frac{\epsilon_1(\lambda_{laser}) C_1 \phi_1 \eta_1(\lambda_{filter1})(1 - \exp[-\epsilon(\lambda_{laser})Ct - \epsilon_2(\lambda_{filter1})C_2 t])\epsilon(\lambda_{laser})C}{\epsilon_2(\lambda_{laser}) C_2 \phi_2 \eta_2(\lambda_{filter2})(1 - \exp[-\epsilon(\lambda_{laser})Ct])[\epsilon(\lambda_{laser})C + \epsilon_2(\lambda_{filter1})C_2]}$$
$$(5.7)$$

The required condition for thickness measurement is that the fluorescence system should be optically thick so that reabsorption is substantial and measurable. The condition for an optically thick system is $\epsilon_2(\lambda_{filter})C_2 >\approx 0[\epsilon(\lambda_{laser})C]$.

Thus for the experimental setup, it is desired to have the emission spectrum of dye 1 be overlapped with the absorption spectrum of dye 2.

5.2 ERLIF Test Setup

The setup of the experiment involves the use of two 12-bit Charged Coupled Device (CCD) cameras mounted on a single lens, a beam expander, a dichroic mirror which separates the laser and fluorescent emission, and mirrors which steer the beam on to the desired location. The laser is a ND:YAG, which emits pulses with a wavelength of 532 nm and a duration of 9 ns. The short duration of each pulse allows instantaneous measurement of the film thickness. The two dyes used are Pyromethene 605 and Pyromethene 650, which are mixed with the oil. The absorption level of Pyromethene 650 is high in the spectrum range of 500-625 nm and the emission level of Pyromethene 605 is high in the range of 525-700 nm, and thus the combination of the dyes give the desired spectrum overlap [12]. The molarity of Pyromethene 605 in the oil-dye mixture is 0.008 mol/L and the molarity of Pyromethene 650 in the mixture is 0.024

mol/L. The interference filter used on camera 1 has a nominal wavelength of 580 nm, and the filter for camera 2 has a nominal wavelength of 610 nm.

The steel material used for the pin, the bushing, and the bushing housing in the test machine is replaced with transparent acrylic material. This allows the laser pulse to reach the film of oil separating the pin and the bushing, and the resulting fluorescence to reach the camera. The beam of the laser is steered to the contact region through the use of a beam expander, a mirror, and a dichroic mirror. The beam expander expands the laser beam by a factor of 4, and at the same time maintains its collimation. The beam is then reflected on to the dichroic mirror by mirror 1 (See Figure 5-2). The dichroic mirror reflects rays with wavelength less than 570 nm, and transmits rays above this wavelength. The mirror is positioned at a 45° angle to the path of the beam, and thus the laser pulse is reflected straight down on to the pin and the oil-dye mixture. The fluorescence of the dyes are above 570 nm, and thus the emitted beams pass through the dichroic mirror and are steered to the camera by mirror 2.

The thickness of the lubricant film is correlated to the angular position and velocity of the pin-joint by triggering the camera with an encoder. Using the encoder, which is attached to the intermediate linkage, the camera is set to trigger after 0.96^{0} of bushing rotation. Thus there are 50 different images taken within one cycle of bushing rotation, each corresponding to a different position. Since the angular velocity of the pin-joint is known for each position (see Figure 5-3), then the velocity-thickness profile of the lubricant can be determined.

The purpose of the initial test run was not to wear the acrylic pin-joint, but to observe the lubricant behavior in the contact zone. Thus the load applied should be below the failure load of the acrylic. The dimensional analysis shown in chapter 3 establishes that the normal load and the modulus of elasticity of the material used are directly proportional. Thus with acrylic having a modulus of elasticity approximately 1/75 of that of steel, the applied load should also be 1/75 of that used with steel. Thus the applied load for the acrylic was kept below 50 lbf in order to insure that the pin-joint would not wear.
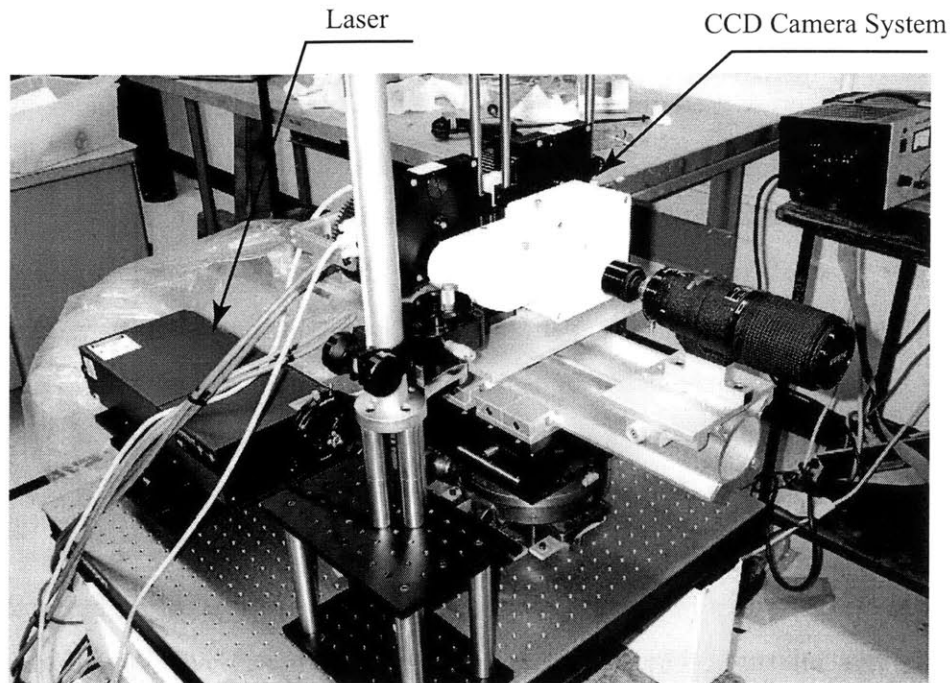
Figure 5-1: Laser and Camera System

The fluorescence of the dye is calibrated by taking images of an oil film with known thickness, which gives a relationship between the film thickness and the fluorescence ratio values. The calibration fixture has been measured previously with a Coordinate Measuring Machine (CMM) to obtain a profile of the thickness (Figure 5-4) [1]. The camera is synchronized with the laser pulse so that the images are taken while the dyes are emitting fluorescence. The images of the contact zone are then taken while the test machine is in operation.

The fluorescent images captured by the CCD cameras are then digitally post-processed by correlating the viewing area of the camera. The cross correlation between the two camera images is done through a Particle Image Velocimetry (PIV) algorithm, which calculates the displacement vector for each pixel. This process will align the images from the two cameras. The ratio of the fluorescent intensity of the correlated images are then taken, which suppresses the intensity fluctuations from the laser.

---

[1]Source: Carlos Hidrovo, Ph.D
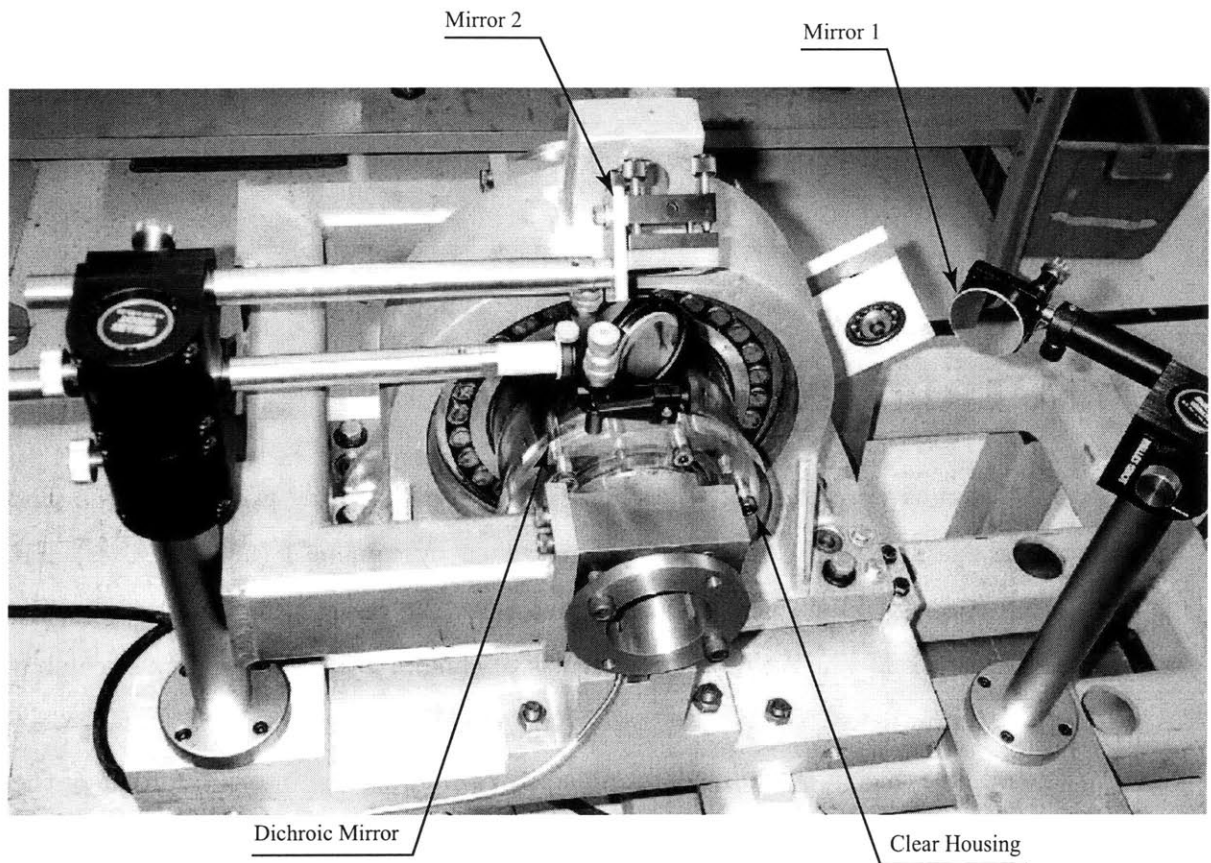
Figure 5-2: Optics
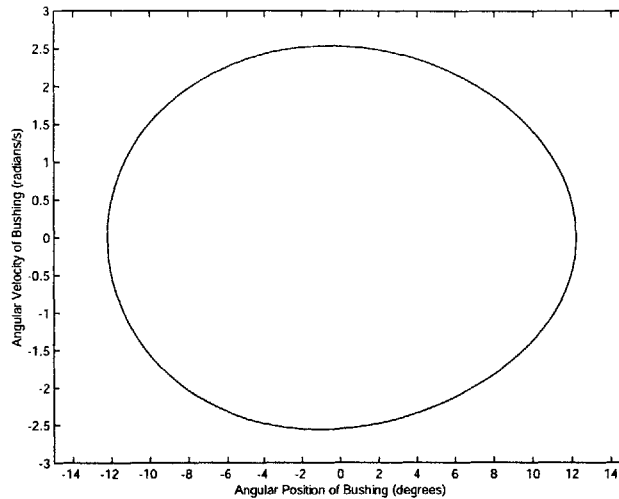
Figure 5-3: Velocity vs Bushing Position

5.3 ERLIF Test Results

Several test runs were conducted, each with a different starting position for the pin-joint. An example of the processed images taken by camera 1 (580 nm filter) and camera 2 (610 nm filter) is shown in Figure 5-5. The images contain the intensity data at each pixel. The ratio of the intensity of camera 2 to the intensity of camera 1 can be seen in figure 5-6.

The oil film thickness can be determined by comparing the intensity profile of the contact zone's processed image to that of the calibration fixture. Using the known thickness profile of the calibration fixture and the processed ERLIF image of the oil film in the fixture, the relationship between the pixel intensity ratio and oil thickness is determined (Figure 5-7, 5-8).

The thickness-intensity relationship is applied to the captured images of the pin-joint contact zone. The lubricant behavior is analyzed by determining the thickness profile in the contact zone. As can be seen in Figure 5-9, the film has the lowest thickness in the contact region which is in the middle of the image. The average thickness value within the image area is calculated and plotted versus the normalized velocity
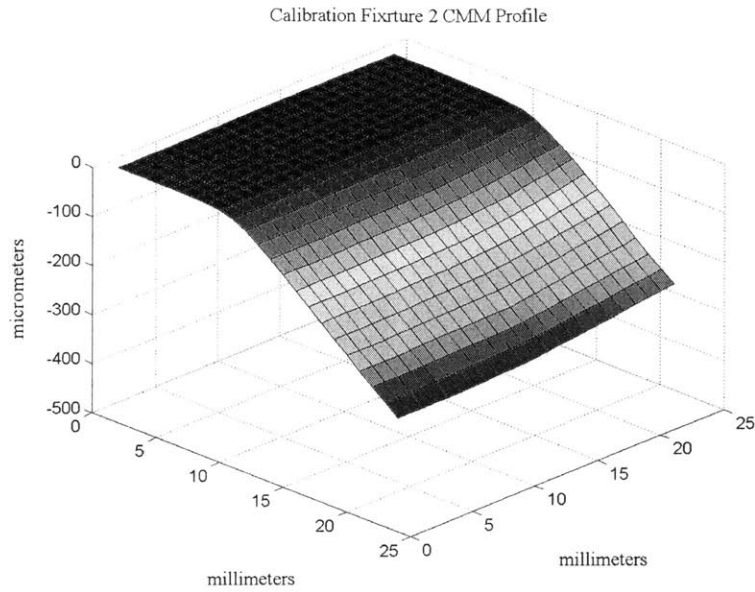
Figure 5-4: CMM Profile of Calibration Fixture

(velocity [radians/second] divided by normal force [lbf]) (Figure 5-10). According to equation 2.8, the minimum film thickness is proportional to velocity/load. Thus the expected trend is an increasing film thickness for an increasing normalized velocity. The trend is not as clear from the experimental data because the noise reduces the resolution of the ERLIF thickness measurements.

Further test with ERLIF will be conducted to analyze the behavior of the lubricant in a lobed bushing. As discussed previously, the contact zone in a lobed bushing is elliptical, compared to a rectangular contact zone in the straight bushing. Thus in order to observe the squeeze out phenomena in the lobed bushing, new tests will need to be conducted.
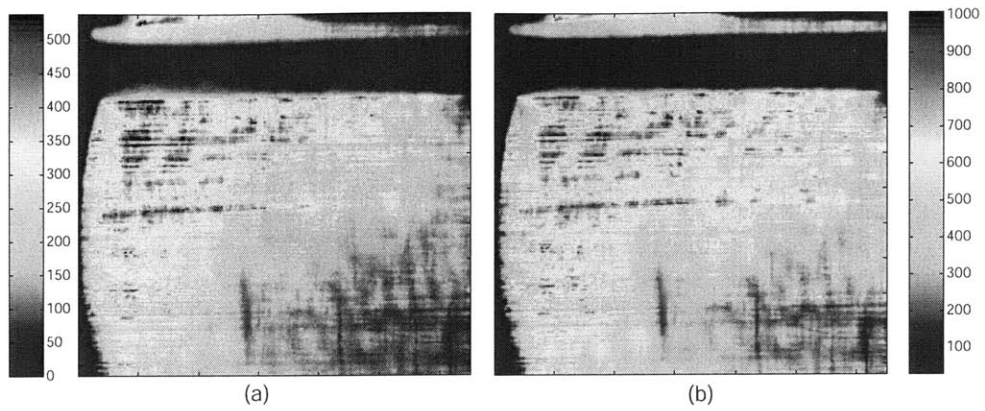
Figure 5-5: Processed Images: (a) 580 nm filter (b) 610 nm filter
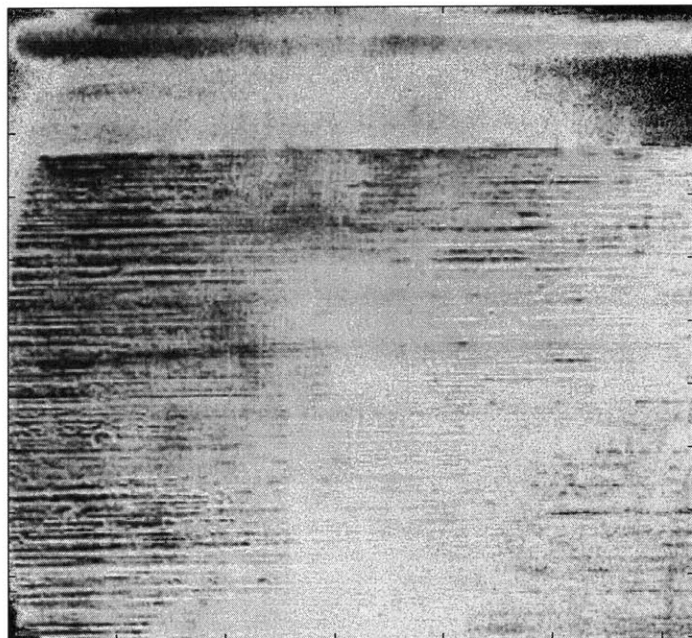
Figure 5-6: Ratio- Image(b) / Image(a)
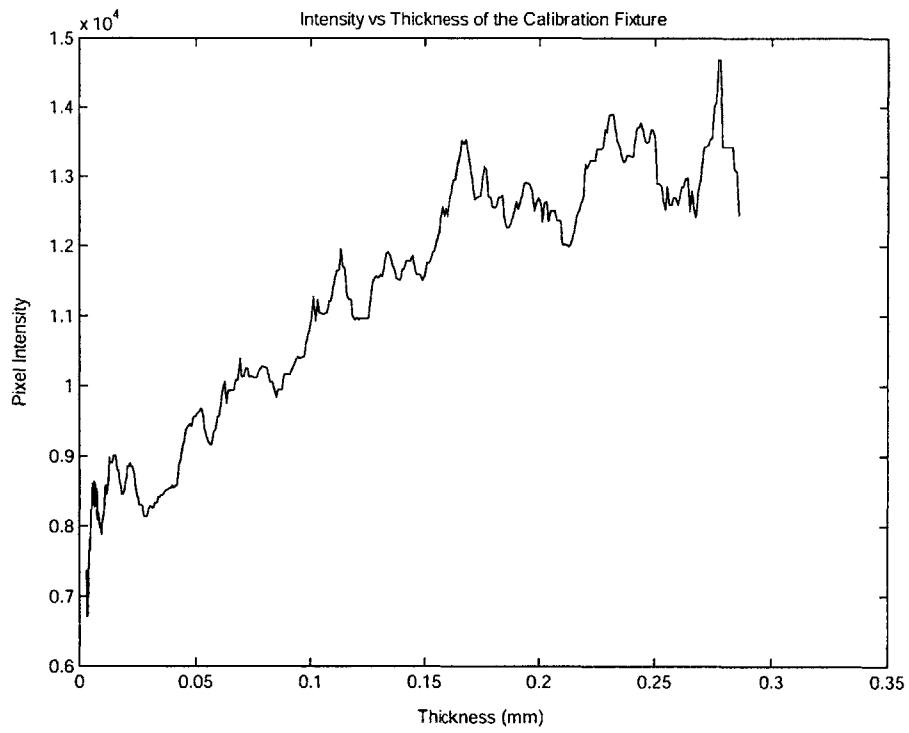
Figure 5-7: Calibration Fixture Intensity-Thickness Relationship
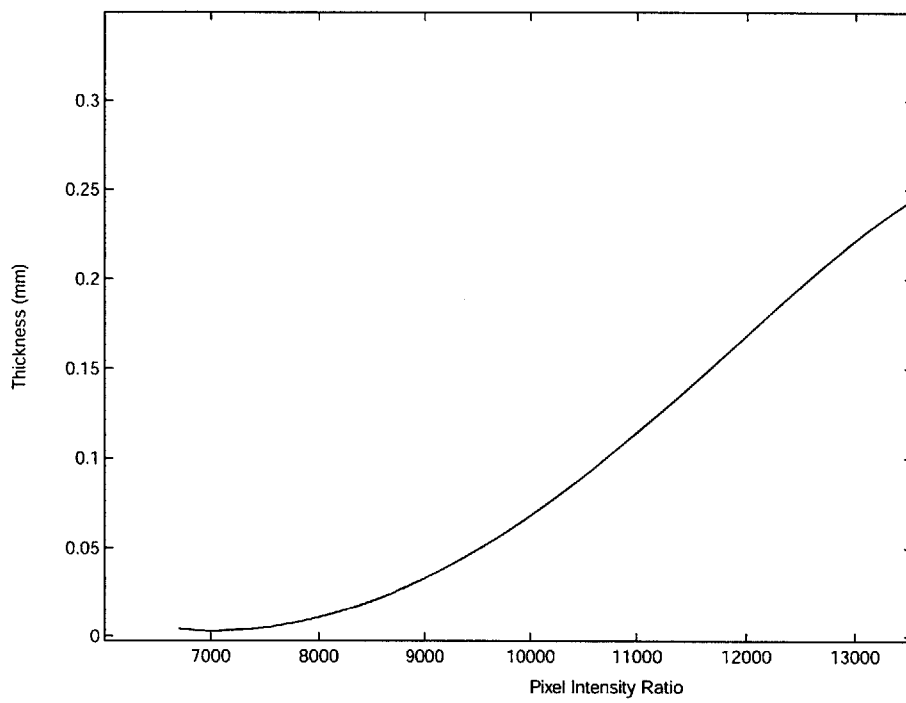
Figure 5-8: Curve fit of Thickness vs Intensity Ratio
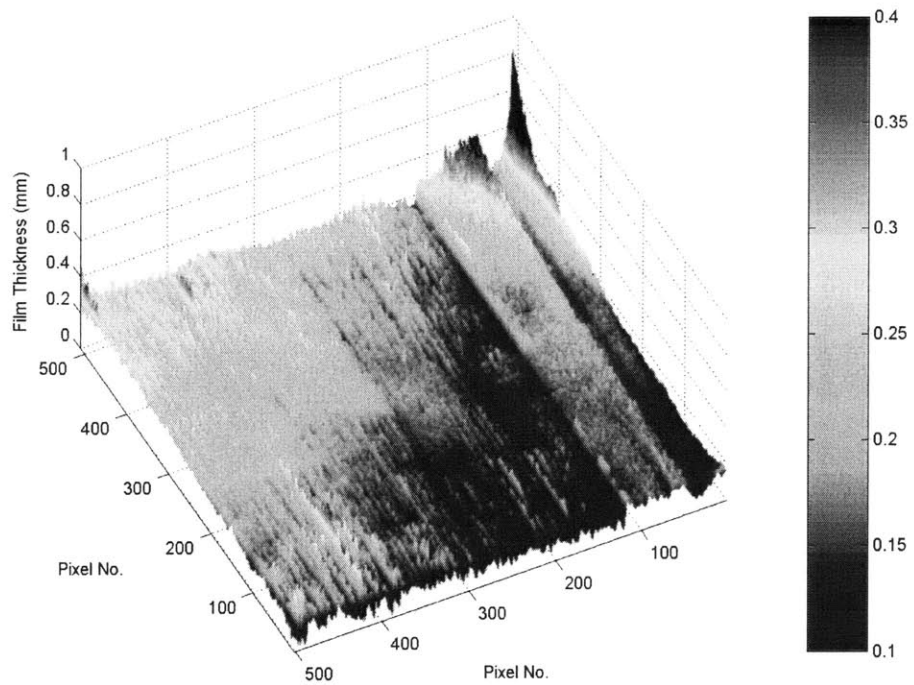
Figure 5-9: Surface Thickness Profile

Normalised velocity Vs Thickness
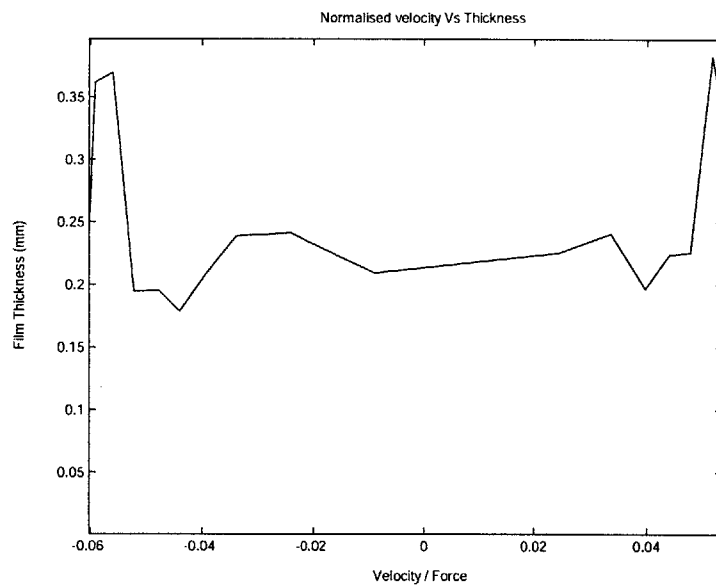
Figure 5-10: Oil Film Thickness vs. Normalized Angular Velocity

Chapter 6

Conclusion

6.1 Contributions

The main failure mechanism associated with pin joints under heavy load is galling, which is caused by high contact stress and poorly lubricated surfaces. The contact stress of the pin joint has been analyzed through both the Hertzian contact model and finite element analysis. The design of the pin joint has been modified by producing an undercut in the bushing. The undercut decreases the contact stress between the pin and the bushing and thus reduces the wear rate. The design of the undercut has been optimized through finite element analysis.

In order to verify the improvement in the new pin joint design, testing was conducted through the use of a test machine. The pin joint was rotated through a crank-rocker mechanism while a normal load was applied. The test results show a longer life for the undercut bushing than the uncut bushing. This supports the theory that the wear rate in the pin-joint will decrease with a reduction in the contact stress.

Optical testing through Emission Reabsorption Laser Induced Fluorescence technique has also been conducted. Through ERLIF, the oil film thickness separating the pin and the bushing can be measured. The film thickness at different sliding speeds and normal loads have been analyzed.

6.2 Future Work

The Hertzian contact model used is a powerful analytical tool that can approximate the contact stress between the pin and the bushing, but further investigation into the validity of the assumptions made for the model should be conducted. Also the Hertzian model should be modified to include the effects of friction and plasticity.

The pin joint testing can be refined by adding an accelerometer in order to better monitor the onset of galling by observing the vibration in the system. Further tests need to be conducted to verify the improvement of the undercut bushing design.

The behavior of the lubricant also needs to be analyzed further. The squeezing of the oil from the contact region should be modelled analytically and compared to the results of the optical test. Further tests through the ERLIF technique should also be conducted to better understand the lubricant behavior.

Appendix A

Design of the Pin Joint Test Machine

In order to determine whether the new designs for the bushing have improved the operational life of the pin joint, it is necessary to design and built a test machine that can test the pin-joint close to its normal operating conditions. One of the operating conditions is that the normal load applied to the pin has to be 100,000 lbf. Also the angle of rotation of the pin in the actual track is approximately 25 degrees; and the maximum speed of rotation of the pin is 2.5 radians per second. The design requirements for the machine include: compactness, ease of operation, and ease of maintenance.

A.1 Mechanism Concepts

In order to achieve the requirement of 25 degrees rotation of the pin at 2.5 radians per second, a feasible mechanism has to be designed which would be easy to implement at minimal cost. Several options were considered, including the use of a hydraulic motor to rotate the pin. The advantage of a hydraulic motor is that it can operate efficiently and can perform with much precision for large loads. The major disadvantage of a hydraulic motor is that it is very expensive since it needs an additional hydraulic pump to operate. It is also very bulky and will take up significant lab space. An

alternative to a hydraulic motor is the use of an electric motor. Unlike a hydraulic motor, the electric motor cannot perform the desired oscillating rotation with the large load. Thus a mechanism needs to be designed where the constant rotation of the motor can be coupled to a rocking motion of the pin. The most feasible way of producing a rocking motion from a constant rotation is through the use of a four-bar linkage.

A.2 Synthesis of the Crank-Rocker Mechanism

The crank-rocker mechanism is a four-bar linkage in which the crank rotates at a constant rotational velocity, producing the rocking of desired link. This mechanism has a single degree of freedom; and according to Grahof's law, the sum of the shortest and longest links of the four-bar linkage cannot be greater than the sum of the remaining two links. The lengths of the linkages are designed so that a full rotation of the crank generates an oscillating rotation of 25-30 degrees for the pin. In order to achieve the desired angle of rotation, a displacement analysis was conducted. For the four-bar linkage, the limits on the angle of the rocker arm can be computed according to [6]

$$\theta_3 = \cos^{-1}\left(\frac{r_3^2 + r_4^2 - r_2^2 - r_1^2}{2r_3r_4} \pm \frac{r_1r_2}{r_3r_4}\right) \tag{A.1}$$

where r_1 through r_4 are defined in Figure A-1.

The geometric constraint in the linkage is that r_4, which is the distance between the pin-joint and the crank, has to be long enough so that there is no interference between the members. Thus for a given r_4 and a desired angle of rotation, the length of the rest of the links can be determined through equation A.1. The necessary distance between the output shaft of the motor and the crank is 51 cm. Through successive iterations the length of the linkages which produce the desired motion are determined. The length of the crank r_1 was determined to be 5.5 cm; the length of the intermediate member r_2 was 44 cm; and the length of the rocker r_3 was determined to be 26 cm. The range of rotation of the rocker is 26^0, which is within the rotational requirement.
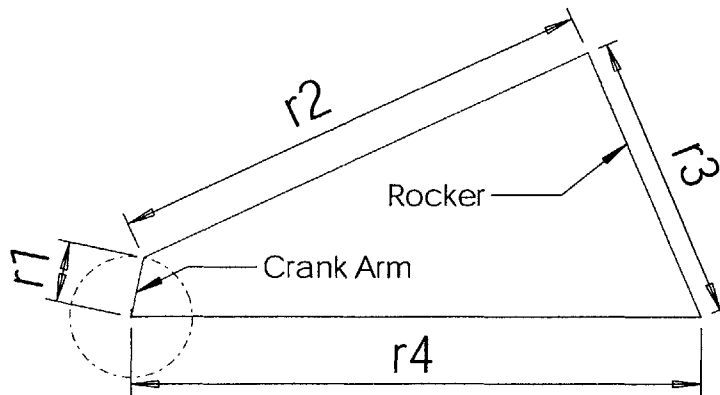
Figure A-1: Crank-Rocker mechanism

In order to meet the velocity requirement, a velocity analysis is conducted to determine the input crank speed that would produce the desired output rocker speed of 24 rpm. The ratio of the maximum rotational velocity of the rocker to the rotational velocity of the crank is equal to the inverse of the ratio of the lengths of the rocker and the crank links. The ratio of r_3 to r_1 is 4.73. Thus it was determined that the crank is to be rotated at a constant rotational speed of 114 rpm in order to produce a maximum rocker velocity of 24 rpm (equivalent to 2.5 radians/s).

A.3 Force and Torque Analysis

The torque necessary to rotate the pin in the bushing can be calculated through friction analysis. The contact friction between the pin and the bushing was modelled as a lubricated steel on steel friction which has a coefficient of friction of approximately 0.15 . The torque can be calculated as T=$\mu F r$, where μ is the friction coefficient, F is the normal force applied to the pin (100,000 lbf), and r is the radius of the pin (1.25 in). Thus the torque necessary to rotate the pin is 2.1 × 10^5 N-cm. Through static analysis, the maximum axial force was determined to be 8.2 kN.

A.4 Design of the Machine Elements

In order to build a functional mechanism, the machine elements involved need to be properly designed. The machine elements include the linkage members, bearings, pin-joints, and motor.

A.4.1 Linkage Design and Bearing Selection

The length of each of the members was determined previously through the crank-rocker analysis. The link which is connected to the bushing-sleeve needs to transmit the force necessary to rotate the pin in the bushing. The maximum axial load on the link is 8.2 kN. The bending stress resulting from this force was calculated to be 37 MPa. The link was designed such that the factor of safety for the link, machined out of Al 6061-T6, is 7. The joint between link r_3 and r_2 needs to rotate freely, thus rolling element bearings are used to minimize the friction at the joint. For this purpose a pin was used to connect link r_2 to two radial ball bearing, manufactured by NTN Co. The dynamic load rating on the ball bearing is 23.9 kN, and thus the life estimated for the bearing was 50,000 hours.[1] The two bearings are press-fit into the housing on the link, and the pin is press-fit through the inner diameter of the bearing. The bearing assembly is over-constrained since the bearing is pressed against a shoulder in the housing on one side and fixed by a bolt attached to the shaft on the other.

The intermediate link r_2 is composed of three components: a rectangular beam, bearing housing, and a threaded rod connecting the two. The component attached to r_3 is a rectangular beam with cross-section of 4.5 cm × 2cm, and is 33 cm long. According to Shigley [19], the stress-concentration of the hole with the pin inside is 2.5, thus giving a maximum stress of 60 MPa around the hole. This gives a factor of safety of 4.5 for the beam.

For ease of assembly, the length of the link is made adjustable through the use of a threaded rod. The threaded rod has a diameter of 1/2 inch and is 10 cm long.

---

[1]$L_{10} = \frac{16667}{N}[\frac{C_E}{P}]^{10/3}; N$: radial speed [rpm]; C_E : Dynamic load rating [Newtons]; P : Normal load [Newtons]

It allows the link to be adjusted by 2 inches. The fatigue strength of the rod was calculated to be 50 MPa. The alternating axial stress in the rod is 16 MPa, thus giving a factor of safety of 3.1. The bearing housing holds a single bearing which allows for rotation around the crank. The bearing is the same type as used in r_3, and has a life of 5000 hours.

The crank is attached to the output shaft of the motor, which rotates at 114 rpm. It is designed to have an adjustable fit on the shaft: it can be clamped on to the shaft by rotating the bolt, which in turn squeezes the crank hole on to the shaft.

A.4.2 Selection of the Motor

To determine the motor size, it was necessary to calculate the torque and the horse-power necessary to rotate the pin-joint. As was previously calculated, the required torque is 2.12×10^5 N-cm. Thus the maximum power necessary to rotate the pin at 24 rpm is 7.1 hp. A survey of the available electric motors showed that a suitable standard rating for the given application is a 7.5 hp motor. The motor chosen for the operation was a helical-bevel geared motor, manufactured by Nord Gear Co [16]. The three-phase motor has an output speed of 114 rpm.

The final assembly of the machine is shown in figure A-2.
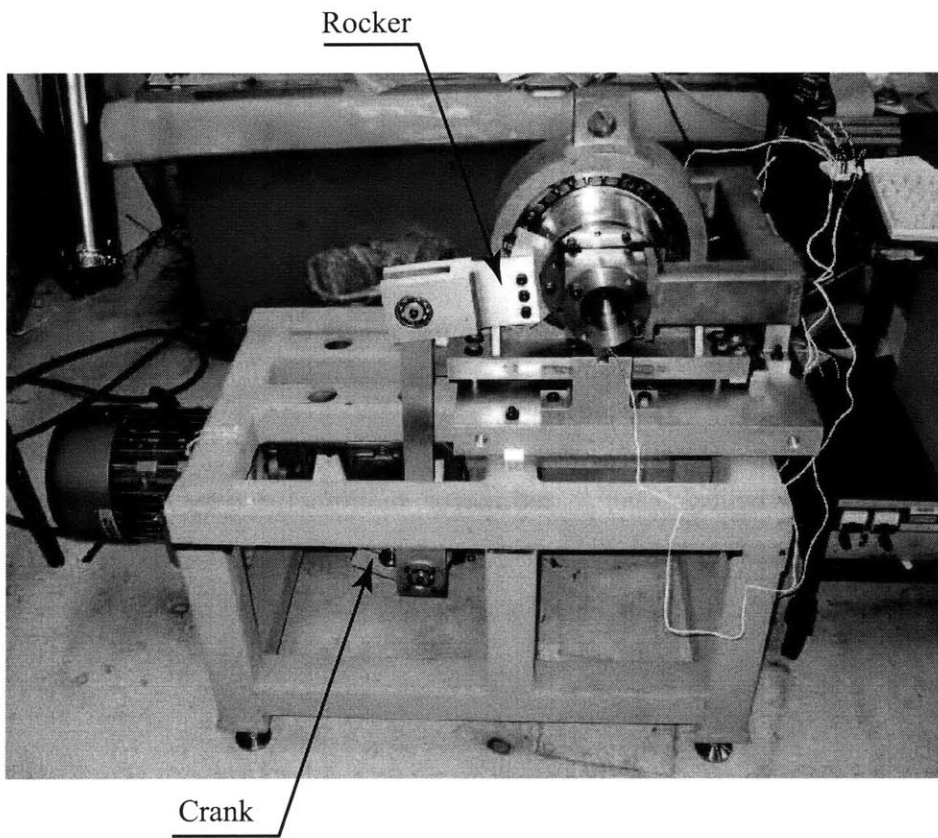
Figure A-2: Test Machine

Figure A-3: Crank
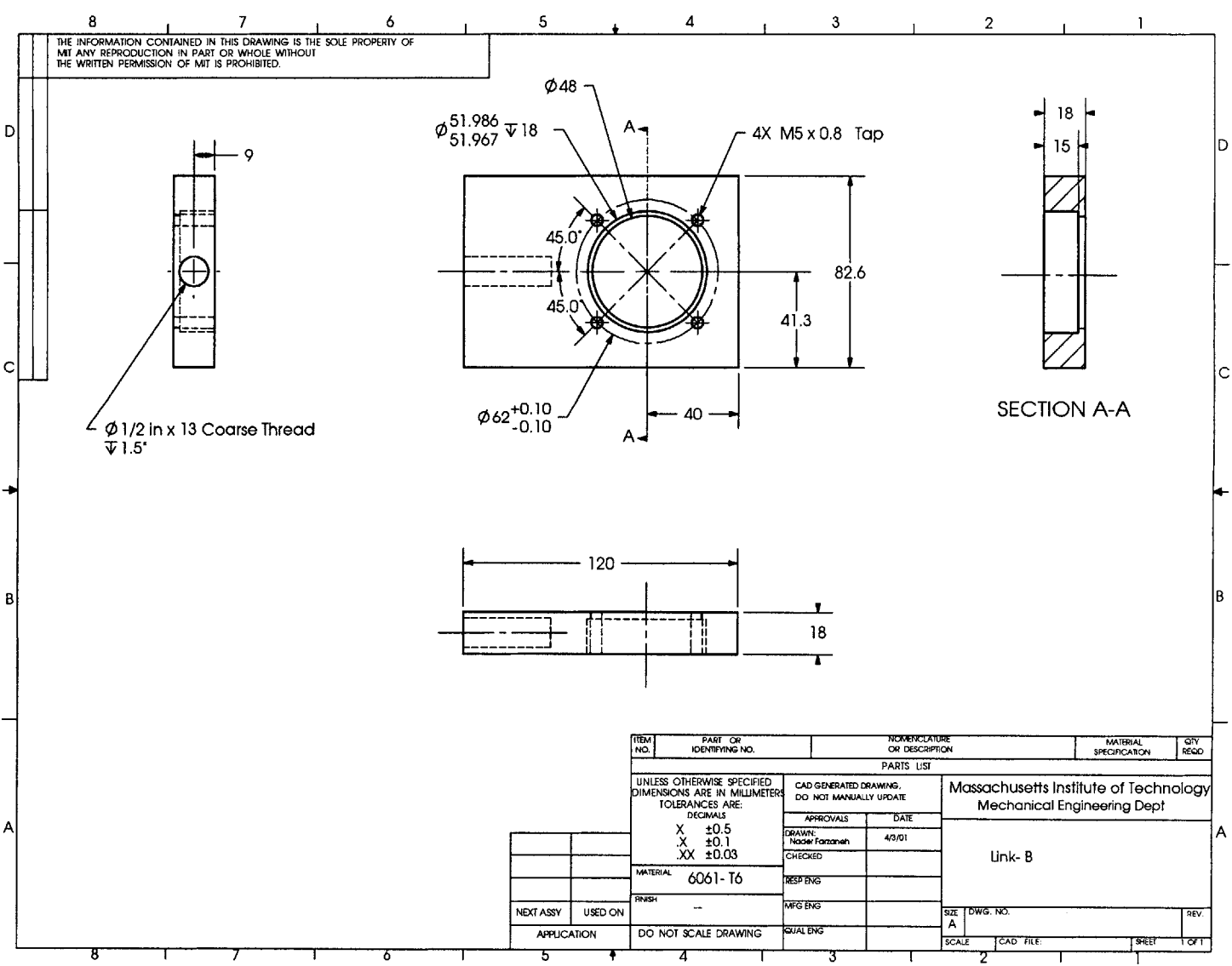
71

METRIC
SCALE

$\phi \begin{smallmatrix} 1.7491 \\ 1.7486 \end{smallmatrix}$

3/8" X 3/8" Key

$\phi 8.5$

135

$\phi 20 \begin{smallmatrix} +0.01 \\ -0.01 \end{smallmatrix}$

3

89

M8x1.25

44.5

55.0

60

150

35

Counterbore $\phi 16$
$\nabla 20$

ITEM NO.	PART OR IDENTIFYING NO.	NOMENCLATURE OR DESCRIPTION	MATERIAL SPECIFICATION	QTY REQD
		PARTS LIST		

UNLESS OTHERWISE SPECIFIED
DIMENSIONS ARE IN MM
TOLERANCES ARE:

CAD GENERATED DRAWING.
DO NOT MANUALLY UPDATE

Massachusetts Institute of Technology
Dept of Mechanical Engineering

X	±0.5	X°	±1°
.X	±0.1	.X°	±0.5°
.XX	±0.03		

APPROVALS	DATE
DRAWN Nader Farzaneh	4/23/01
CHECKED	
RESP ENG	
MFG ENG	
QUAL ENG	

Crank

MATERIAL
6061-T6

FINISH

SIZE A | DWG. NO. | REV.

CAD FILE:

SHEET 1 OF 1

Figure A-4: Fork Link

72

THE INFORMATION CONTAINED IN THIS DRAWING IS THE SOLE PROPERTY OF
MIT ANY REPRODUCTION IN PART OR WHOLE WITHOUT
THE WRITTEN PERMISSION OF MIT IS PROHIBITED.

Ø48 Thru

$\phi \begin{smallmatrix} 51.986 \\ 51.967 \end{smallmatrix}$ ⊽15

3xØ13

R5

2xR10

PARTS LIST

UNLESS OTHERWISE SPECIFIED DIMENSIONS ARE IN MILLIMETERS TOLERANCES ARE: DECIMALS	CAD GENERATED DRAWING. DO NOT MANUALLY UPDATE		Massachusetts Institute of Technology Mechanical Engineering Dept		
X ±0.5 .X ±0.1 .XX ±0.03	APPROVALS	DATE			
	DRAWN Nader Farzaneh	4/23/01			
	CHECKED		Fork Link		
MATERIAL 6061-T6	RESP ENG				
FINISH --	MFG ENG				
NEXT ASSY	USED ON			SIZE A	DWG. NO.	REV.
APPLICATION	DO NOT SCALE DRAWING	QUAL ENG		SCALE	CAD FILE:	SHEET 1 OF 1

Figure A-5: Link A

73

Ø 1/2 in x 13 Coarse Thread
▽ 1.5"

10

Ø20 +0.01 -0.01 Thru

4. 5

22.2

20

332

20

ITEM NO.	PART OR IDENTIFYING NO.	NOMENCLATURE OR DESCRIPTION		MATERIAL SPECIFICATION	QTY REQD
		PARTS LIST			

UNLESS OTHERWISE SPECIFIED
DIMENSIONS ARE IN MILLIMETERS
TOLERANCES ARE:
DECIMALS
X   ±0.5
.X   ±0.1
.XX   ±0.03

MATERIAL
6061-T6

FINISH
—

NEXT ASSY	USED ON
APPLICATION	

CAD GENERATED DRAWING.
DO NOT MANUALLY UPDATE

	APPROVALS	DATE
DRAWN	Nader farzaneh	4/23/01
CHECKED		
RESP ENG		
MFG ENG		
QUAL ENG		

DO NOT SCALE DRAWING

Massachusetts Institute of Technology
Mechanical Engineering Dept

Link A

SIZE A	DWG. NO.		REV.
SCALE	CAD FILE:	SHEET 1 OF 1	

Figure A-6: Link B

74

9

Ø48

Ø $^{51.986}_{51.967}$ ⤵18

A

4X M5 x 0.8 Tap

45.0°

45.0°

82.6

41.3

Ø62 $^{+0.10}_{-0.10}$

40

A

Ø1/2 in x 13 Coarse Thread
⤵1.5"

18
15

SECTION A-A

120

18

ITEM NO.	PART OR IDENTIFYING NO.		NOMENCLATURE OR DESCRIPTION	MATERIAL SPECIFICATION	QTY REQD
			PARTS LIST		

UNLESS OTHERWISE SPECIFIED DIMENSIONS ARE IN MILLIMETERS TOLERANCES ARE:

DECIMALS

X ±0.5
.X ±0.1
.XX ±0.03

MATERIAL
6061-T6

CAD GENERATED DRAWING,
DO NOT MANUALLY UPDATE

APPROVALS	DATE
DRAWN: Nader Farzaneh	4/3/01
CHECKED	
RESP ENG	
MFG ENG	
QUAL ENG	

Massachusetts Institute of Technology
Mechanical Engineering Dept

Link- B

NEXT ASSY   USED ON

FINISH --

APPLICATION

DO NOT SCALE DRAWING

SIZE A   DWG. NO.   REV.

SCALE   CAD FILE: SHEET 1 OF 1

Figure A-7: Ring

75

4 X ϕ5.5, Thru

ϕ46

ϕ62$^{+0.10}_{-0.10}$

ϕ75

5

ITEM NO.	PART OR IDENTIFYING NO.	NOMENCLATURE OR DESCRIPTION	MATERIAL SPECIFICATION	QTY REQD
		PARTS LIST		

UNLESS OTHERWISE SPECIFIED DIMENSIONS ARE IN MILLIMETERS TOLERANCES ARE:
DECIMALS
X ±0.5
.X ±0.1
.XX ±0.03

CAD GENERATED DRAWING, DO NOT MANUALLY UPDATE

Massachusetts Institute of Technology
Mechanical Engineering Dept

	APPROVALS	DATE
DRAWN: Nader Farzaneh		4/3/01
CHECKED		
RESP ENG		
MFG ENG		
QUAL ENG		

MATERIAL 6061-T6

FINISH —

Ring

NEXT ASSY	USED ON
APPLICATION	

DO NOT SCALE DRAWING

SIZE A | DWG. NO. | REV.

SCALE | CAD FILE: | SHEET 1 OF 1

Appendix B

Hertz Contact Stress

The contact of the bushing lobe against the straight pin results in an elliptical region of contact. The pin and the bushing are conformal bodies, but the lobe of the bushing does not conform to the surface of the pin. In order to determine whether the Hertzian model of contact can be applied to this case, an initial estimate of the contact area and the contact pressure was calculated as follows:

Dimensions of the pin and the bushing:

Radius of the bushing $R_1' = -33.59$ mm (negative since it is concave with respect to the pin)

Radius of the bushing lobe $R_1'' = 200$ mm

Radius of the pin $R_2' = 33.36$ mm

Radius of pin lobe $R_2'' = \infty$ (straight cylinder)

Equivalent Modulus of Elasticity:

$$E^* = (\frac{1 - \nu_1^2}{E_1} + \frac{1 - \nu_2^2}{E_2})^{-1} \tag{B.1}$$

where $E_1 = E_2 = 200$ GPa, $\nu_1 = \nu_2 = 0.3$

Equivalent Radius:

$$R_{eq} = \sqrt{R' \times R''} \tag{B.2}$$

$$A + B = \tfrac{1}{2}(\tfrac{1}{R_1'} + \tfrac{1}{R_1''} + \tfrac{1}{R_2'} + \tfrac{1}{R_2''}) \tag{B.3}$$

$$B - A = \tfrac{1}{2}\{(\tfrac{1}{R_1'} - \tfrac{1}{R_1''})^2 + (\tfrac{1}{R_2'} - \tfrac{1}{R_2''})^2 + 2(\tfrac{1}{R_1'} - \tfrac{1}{R_1''})(\tfrac{1}{R_2'} - \tfrac{1}{R_2''})\cos 2\theta\}^{\frac{1}{2}} \tag{B.4}$$

The axes of the pin and the bushing are aligned, thus $\theta = 0$.

$$\frac{1}{R'} = \frac{1}{R_1'} + \frac{1}{R_2'} \tag{B.5}$$

$$\frac{1}{R''} = \frac{1}{R_1''} + \frac{1}{R_2''} \tag{B.6}$$

Since $R_2'' = \infty$, then $R'' = R_1''$.

$$c = \sqrt{ab} = \left(\frac{3PR_{eq}}{4E^*}\right)^{\frac{1}{3}} F_1 \tag{B.7}$$

where P is the applied load

$$\frac{a}{b} \approx \left(\frac{R'}{R''}\right)^{\frac{2}{3}} \tag{B.8}$$

and solving for b

$$b = \left(\frac{3PR_e R_1''}{4E^* R'}\right)^{\frac{1}{3}} F_1 \tag{B.9}$$

Maximum Contact Pressure:

$$P_0 = \frac{3P}{2\pi ab} = \left(\frac{6PE^{*2}}{\pi^3 R_{eq}^2}\right) F_1^{-\frac{2}{3}} \tag{B.10}$$

Distance of the deformation:

$$\delta = \left(\frac{9P^2}{16R_{eq}E^{*2}}\right)^{\frac{1}{3}} \times F_2 \tag{B.11}$$

The functions F_1 and F_2 are correction factors that allow for the eccentricity of the ellipse, and their value are 0.89 and 0.88 respectively [14]. For a total applied load of 100,000 lbf (50,000 lbf per lobe), the maximum contact pressure P_0 is 1024 MPa. The length of the major axis of the contact ellipse a is 30 mm and the length of the minor axis b is 3.5 mm. The resulting deformation δ is 0.12 mm.
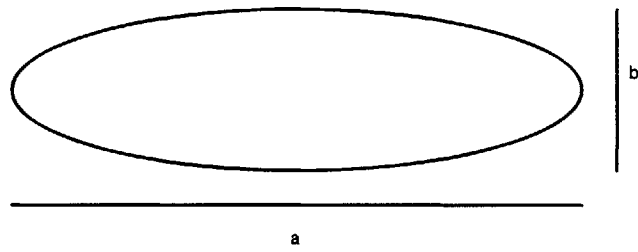
Figure B-1: Elliptical Hertzian Contact Region

Appendix C

Assembly Procedure

[1]

1. Cleaning:

   (a) Clean pin and bushing surfaces

   (b) Clean all taper surfaces (bushing housing, pin clamps, bushing clamps, pin connector).

2. Lubrication:

   (a) Grease seal spacers.

   (b) Grease O rings.

   (c) Grease red lip of seal.

   (d) Grease spherical bearing rollers. The most important rollers are the ones located at the top of the ring near the eye (used for moving the housing).

3. Assembly:

   (a) Flexures to Bearing Housing:

---

[1]Written with Greg Radighieri

i. Fasten the flexures to the bearing housing but not to the support base. Do not tighten them yet. Note: You may have to lay the bearing housing on it's side to do this.

ii. Slide the bearing housing on the support base in between the pin supports. The housing should be slightly angled and partly overhanging the support base (because of the flexures on one end). This will make assembly easier for the "C" piece.

iii. Place 100,000lbf load cells in each support pin's locating hole.

(b) Bushing into Bushing Housing:

i. Insert bushing into bushing housing.

ii. Insert bushing clamps but do not clamp them yet.

iii. Center bushing inside bushing housing.

iv. Begin to hand tighten bushing clamps. Make sure the bushing remains centered while tightening.

v. Tighten bushing clamps with wrench (again, make sure the bushing remains centered). Make sure to tighten bolts uniformly to prevent the clamp taper from prematurely grasping the bushing housing or the bushing.

(c) Bushing Housing Mount:

i. Fasten the bushing housing mount (curved piece with 4 radial holes and 3 axial holes) to the bushing housing.

ii. Tighten bushing housing mount.

(d) Seal Preloading:

i. Completely assemble and tighten one pin connector to the "C" Piece. Note: The threaded holes located on the taper face should be facing away from the rest of the "C" piece.

ii. Insert pin into bushing

iii. Insert seal, black lip facing the bushing, on each side.

iv. Insert one plain (thin) seal spacer on each side. Insert shouldered spacer at each end. Shoulder should face away from the bushing.

v. Insert one O ring on each side.

vi. Slide one side of the pin almost completely into the bushing. The O ring should be visible.

vii. Place the fastened pin connector's large bore hole over the barely visible side of the pin. Note: You may have to remove a few bolts from the bushing clamp on the opposite side of the bushing to get this to happen. Also, you may need to tighten the bushing clamps more.

viii. Carefully slide the pin into the pin connector. Note that the O ring will likely get stuck on the lip of the connector. If so, stop pushing the pin. Push the caught portion of the O ring back toward the bushing while pushing the pin from the opposite side of the bushing.

ix. If the bearing housing is positioned correctly, you should be able to rest the "C" Piece on the two 100,000lbf load cells.

x. Center the pin , and place the other pin connector on the pin. Be careful, it is loose and should be immediately held on with the preload blocks.

xi. Attach the two preload blocks. This is simply a block of Aluminum with two through holes. Press one block face against the face of a pin connector, aligning the block holes with those of the nearest bushing clamp. Pass two long M8 bolts through the block holes to the two threaded holes on the bushing clamp. Note: It may help to have one person maneuver the "C" piece while attaching the preload blocks.

xii. Lightly preload each block. Note: For the loose pin connector, try centering the connector (with respect to the pin axis) with one hand while lightly preloading with the other hand. This will make the next part easier.

xiii. The goal now is to align the holes on the loose pin connector. Increase

the preload. Alternate blocks while doing so. Meanwhile, check the hole alignment. Once the holes are aligned, insert 4 M8's, and tighten them completely. Make sure all 8 M8's on the "C" piece are firmly tightened.

    xiv. Remove preload blocks.

(e) Cut-Head Bolts:

    i. Position bushing housing mount such that it is near its linkage with the electric motor.

    ii. More than likely, one side of the "C" piece will be closer to the corresponding bushing clamp than the other. If so, the bolt heads close to the "C" piece should be replaced with cut-head bolts. Note that the bushing housing will rotate will rotate through about 30degrees total. In this rotation, there should be at most three bolt heads (on the crowded side) that may interfere with the rotation. Replace these bolts with cut-head bolts. I simply used a grinder to shave some thickness off the heads.

(f) Placing Assembly on Load Cells:

    i. Make sure third load cell support is affixed to support base. Make sure third load cell is hand tightened into this support. Using THREE people, place the assembly onto the load cells. Use two people, one on each side of the assembly, and a steel pipe through the bearing housing eye to lift the assembly. The third person should guide hold onto the "C" piece with both hands, guiding the large bore "C" piece onto the third load cell. The bottoms of the pin connectors should contact the 100,000lbf load cells.

(g) Bolt Array

    i. Align the bolt array holes on the bearing housing with the support base holes. Place the blue M12's into all ten holes, partially fastening them to the nuts on the underside of the support base.

(h) Attach Fork Link to Bushing Housing Mount:

 i. Guided by dowel pins, place two spacers onto the fork link.

 ii. Align the dowel pins with the corresponding holes on the bushing housing mount. This can be done by rotating the bushing housing with the bushing housing mount while holding the fork link.

 iii. Place two spacing blocks (steel block with 3 clearance holes) on the opposite side of the fork link, and clamp them firmly with three M10's.

(i) Fastening and Positioning:

 i. Place the flexure pieces on the support base. Each side should include one aluminum block with two through holes. There are also two shim pieces. Level the bearing housing and place the shims where necessary. Usually, only one is needed.

 ii. Place a flexure cap (slightly smaller than the flexure block) over each flexure blade and tighten firmly.

 iii. Fasten and firmly tighten a washer and a nut on the third load cell.

 iv. Using a torque wrench, tighten the bolt array as desired. Note that the preload distance is small and easy to unload; hence, I recommend you tighten each group of 5 and then the other group. Repeat this process one more time to ensure uniform preloading.

Bibliography

[1] Andreasen, J.L., Bay, N., Chiffre, L. De; 1998, "Quantification of Galling in Sheet Metal Forming by Surface Topography Characterisation", *International Journal of Machine Tool Manufacturing*, Vol 38, Nos 5-6, pp. 503-510.

[2] Bhansali, K.J., Miller, A.E.; 1982, "The Role of Stacking Fault Energy on Galling and Wear Behavior", *Wear*, Vol 75, pp. 241-252.

[3] Budinski, Kenneth G.; 1981, "Incipient Galling of Metals", *Wear*, Vol 74, pp. 93-105.

[4] Budinski, Kenneth G.; 1988, *Surface Engineering for Wear Resistance*. Englewood: Prentice Hall.

[5] Cann, P.M., Spike, H.A.; 1989, "Determination of the Shear Stress of Lubricants in Elastrohydrodynamic Contacts", *Triblogy Transactions*, Vol 32-3, pp. 414-422.

[6] Erdman, Arthur G.; 1997, *Mechanism Design : Analysis and Synthesis*. Upper Saddle River, N.J. : Prentice Hall.

[7] Fay, James A.; 1994, *Introduction to Fluid Mechanics* Cambridge: MIT Press.

[8] Fein, Richard S.; 1991, "Boundary Lubrication", *Journal of the Society of Tribologists and Lubrication Engineers*, pp. 1005-1008.

[9] Hamrock, Bernard J., Jacobson, Bo O., Schmid, Steven R.; 1999, *Fundamentals of Machine Elements* Boston : WCB/McGraw-Hill.

[10] Hidrovo, Carlos H. Hart, Douglas P.; 2001, "Emission Reabsorption Laser Induced Fluorescence Film Thickness Measurement", *Measurement Science and Technology*, Vol 12, pp. 467-477.

[11] Hidrovo, Carlos H. Hart, Douglas P.; 1999, "Development of a Dual Purpose Visualization Technique for the Study of Rotating Shaft Seals", *Proceedings of the 3rd ASME/JSME Joint Fluids Engineering Conference July 18-23, 1999, San Francisco, California.*

[12] Hidrovo, Carlos H; 2001, *Ph.D Thesis, Mechanical Engineering Department, MIT, Cambridge, Massachusetts.* "Development of a Fluorescence Based Optical Diagnostics Technique and Investigation of Particle Ingestion and Accumulation in the Contact Region of Rotating Shaft Seals".

[13] Hopkins, Daniel N., Harrington, Craig D., Black, Bill R.; 1999, "Reduce Maintenance Costs by Using Engineered Surfaces to Control Friction and Galling", *Wear*, Vol 225-229, pp. 27-37.

[14] Johnson, K.L.; 1985, *Contact Mechanics.* Cambridge University Press.

[15] Markov, D., Kelly, D.; 1999, "Mechanism of Adhesion-initiated Catastrophic Wear: Pure Sliding", *Wear*, Vol 239, pp. 189-210.

[16] Nord Gear Co.; Waunakee, WI.

[17] Rabinowicz, E; 1973, "Friction Seizure and Galling Seizure", *Wear*, Vol 25, pp. 357-363.

[18] "Solver Formulations: The contact Algorithms Used by the Solvers" *SDRC User Manual.*

[19] Shigley, Joseph Edward, Mischke, Charles R.; 1989, *Mechanical Engineering Design.* Ney York: McGraw-Hill.

[20] Stachowiak, Gweidon W; Batchelor, Andrew W; 2001, *Engineering Tribology.* Boston: Butterworth-Heinemann.

[21] Stolarski, T. A.; 1990, *Tribology in Machine Design.* Oxford : Heinemann Newnes.

[22] Tallian, T.E.; 1967, "Rolling Contact Failure Control Through Lubrication", *Lubrication and Wear: Fundamentals and Application to Design, Proceedings of the Institution of Mechanical Engineers*, Vol 182, Part 3A, pp. 205-236.

[23] Wiklund, U., Hutchings, I.M.; 2001, "Investigation of Surface Treatments for Galling Protection of Titanium Alloys", *Wear*, Vol 251, pp. 1034-1041.